



**CHARACTERIZATION OF THE OPTICAL AND  
ELECTRICAL PROPERTIES OF PROTON-  
IRRADIATED 4H-SILICON CARBIDE**

THESIS

Heather C. Crockett, Second Lieutenant, USAF

AFIT/GNE/ENP/02M-01

**DEPARTMENT OF THE AIR FORCE  
AIR UNIVERSITY**

**AIR FORCE INSTITUTE OF TECHNOLOGY**

---

---

**Wright-Patterson Air Force Base, Ohio**

APPROVED FOR PUBLIC RELEASE; DISTRIBUTION UNLIMITED.

The views expressed in this thesis are those of the author and do not reflect the official policy or position of the United States Air Force, Department of Defense, or the U.S. Government.

AFIT/GNE/ENP/02M-01

CHARACTERIZATION OF THE OPTICAL AND ELECTRICAL PROPERTIES OF  
PROTON-IRRADIATED 4H-SILICON CARBIDE

THESIS

Presented to the Faculty of the Graduate School of Engineering and Management

of the Air Force Institute of Technology

Air University

Air Education and Training Command

In Partial Fulfillment of the Requirements for the  
Degree of Master of Science in Nuclear Engineering

Heather C. Crockett, BSNE

Second Lieutenant, USAF

26 March 2002

APPROVED FOR PUBLIC RELEASE; DISTRIBUTION UNLIMITED

CHARACTERIZATION OF THE OPTICAL AND ELECTRICAL PROPERTIES OF  
PROTON-IRRADIATED 4H-SILICON CARBIDE

Heather C. Crockett, BSNE  
Second Lieutenant, USAF

Approved:



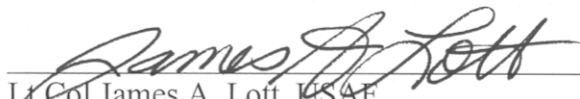
Maj Michael B. Scott, USAF  
Assistant Professor of Physics  
Department of Engineering Physics  
Chairman, Advisory Committee

3/6/02  
date



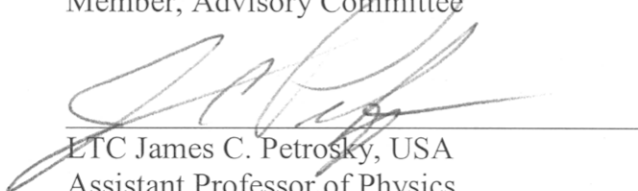
Dr. Robert L. Hengehold  
Professor of Physics  
Department of Engineering Physics  
Member, Advisory Committee

3/6/02  
date



Lt Col James A. Lott, USAF  
Professor of Electrical Engineering  
Department of Electrical and Computer Engineering  
Member, Advisory Committee

6 MARCH 2002  
date



ETC James C. Petrosky, USA  
Assistant Professor of Physics  
Department of Engineering Physics  
Member, Advisory Committee

06 MAR 02  
date

## Acknowledgments

I would like to take this opportunity to express my gratitude to all the people who aided in the completion of my research. First of all, my thanks and appreciation goes to my advisor, Maj Michael Scott, a man I truly respect and admire, for all the guidance he has afforded me in the areas of SiC material and semiconductor characterization. Also, thanks goes to LTC James Petrosky, not only for his guidance in the area of radiation effects in electronics but also for his great help in coordinating the resources necessary to complete the irradiation of my SiC samples. All the proton irradiation work was completed at the Edwards Accelerator Facility, Ohio University under the direction of Dr. David Ingram and his wonderful team of associates. His knowledge of radiation dosimetry and general understanding of the kinetics of protons in materials helped to make this research a success. Finally, I must express my deepest appreciation to Mr. Greg Smith. Without his technical expertise, this research would not even get off the ground.

Heather C. Crockett

*“I have no special talents. I am only passionately curious.”  
~Albert Einstein~*

# Table of Contents

	Page
Acknowledgments.....	iv
List of Figures .....	vi
List of Tables.....	viii
Abstract .....	ix
Chapter I : Overview of Silicon Carbide Material.....	1
Introduction .....	1
Purpose of Research.....	3
Thesis Organization .....	6
Chapter II : Silicon Carbide Material Characteristics and Damage Effects...	7
Physical and Material Characteristics of Silicon Carbide.....	7
Effects of Heavy-Charged Particle Radiation .....	12
Effects of Damage on the Material Characteristics.....	14
Effects of High-Temperature Annealing.....	16
Chapter III : Methods of Semiconductor Characterization.....	18
Photoluminescence Spectroscopy .....	18
I-V Diode Characterization .....	24
Deep Level Transient Spectroscopy.....	25
Chapter IV : Material and Experimental Resources.....	32
4H-SiC Material.....	32
Proton Irradiation Sequence.....	35
Contact Fabrication .....	37
High-Temperature Annealing .....	38
Experimental Apparatus Set-up .....	39
Chapter V : Data Analysis and Results.....	43
Photoluminescence Spectroscopy Data Analysis.....	44
Electrical and Deep Level Transient Spectroscopy Data Analysis .....	54
Chapter VI : Conclusions and Closing Remarks.....	64
Summary of Conclusions .....	64
Proposals for Future Research .....	66
Appendix: Photolithography Processing and Metallization.....	69
Bibliography.....	72
Vita.....	74

## List of Figures

Figure 1: Distribution of trapped protons with energy greater than 1 MeV .....	4
Figure 2: SiC tetrahedral covalent bond structure.....	8
Figure 3: (a) Triangular grid structure of a SiC bilayer (b) ABCABC SiC crystal lattice structure (c) ABAB SiC crystal lattice structure (All as viewed along the c-axis).....	8
Figure 4: (a) Pure zincblende (3C-SiC) crystal symmetry (b) Pure wurtzite (2H-SiC) crystal symmetry (c) Quasi-hexagonal (4H-SiC) crystal bonding structure .....	10
Figure 5: Most common radiative transitions observable with photoluminescence .....	20
Figure 6: Photoluminescence spectra of as-grown n-type (nitrogen-doped) 4H-SiC .....	22
Figure 7: Rate window concept of boxcar DLTS. A series of C-t curves, at different temperatures, for a given gate setting $t_1$ and $t_2$ , are analyzed to determine the characteristic emission time constant.....	30
Figure 8: 4H-SiC sample layout on the stainless steel finger. A 2 MeV proton beam is stepped across the samples to irradiate the material uniformly. ....	36
Figure 9: (a) A series of Gaussian curves represents the 25x50 mm beam aperture as it steps across the samples to produce a uniform dose in the 4H-SiC material (b) 4H-SiC sample orientation with respect to incoming proton beam .....	37
Figure 10: Photoluminescence laboratory set-up.....	40
Figure 11: Deep level transient spectroscopy laboratory set-up .....	41
Figure 12: Photoluminescence spectra of as-grown epitaxial n-type 4H-SiC. The zero phonon lines (ZPLs) and several corresponding phonon replicas associated with the neutral nitrogen complex are listed. ....	45
Figure 13: The lattice-related phonon energies of 38, 76, 94, and 106 meV detected by photoluminescence measurements of the n-type 4H-SiC material (shown at right). The curves shown are reproduced from Feldman for the phonon energies for 4H-SiC along the c-axis. ....	47
Figure 14: Constant-temperature photoluminescence spectra of n-type 4H-SiC epilayers irradiated by 2 MeV protons (dose $\sim 1.5 \times 10^{14}$ cm <sup>-2</sup> ) and subsequently annealed for 20 minutes at several temperatures. The spectra are offset for clarity.....	48
Figure 15: Photoluminescence spectra of irradiated n-type 4H-SiC after subsequent high-temperature annealing at several temperatures. The spectra are offset for clarity.....	50

Figure 16: Constant-temperature photoluminescence spectra of as-grown and irradiated epitaxial n-type 4H-SiC. Note the effect of high-temperature annealing (1500 °C) in the recovery of the intrinsic near-band edge phonon structure. ....	52
Figure 17: Rectifying behavior of irradiated n-type 4H-SiC followed by thermal annealing at several temperatures .....	55
Figure 18: DLTS response curve of n-type 4H-SiC illustrating the emergence of deep centers as a result of proton irradiation. Note the decrease in peak signal as a result of high-temperature annealing. ....	58
Figure 19: DLTS response curve for n-type 4H-SiC material, irradiated and annealed at 1100 °C. Using a manual curve-fitting algorithm, the data peak is resolved into six individual trapping centers. The associated trap parameters, ( $E_T$ , $\sigma_T$ , $N_T$ ) for each defect peak are listed at right. ....	60

## **List of Tables**

Table 1: Electrical and optical characteristics of various semiconductor materials .....	11
Table 2: Cree <sup>®</sup> research-grade wafers used for this study .....	33
Table 3: Sample matrix for comprehensive proton irradiation/anneal study .....	35
Table 4: Thermal anneal study matrix.....	39
Table 5: Trap parameters of proton-irradiated n-type 4H-SiC prior to thermal anneal ...	61
Table 6: Trap parameters of proton-irradiated n-type 4H-SiC annealed at 900 °C .....	61
Table 7: Trap parameters of proton-irradiated n-type 4H-SiC annealed at 1100 °C .....	61
Table 8: Trap parameters of proton-irradiated n-type 4H-SiC annealed at 1500 °C .....	61

## Abstract

Epitaxial n-type 4H-silicon carbide (SiC) is irradiated with 2 MeV protons to evaluate the dislocation damage effects on the optical and electrical characteristics of the material. Semiconductor materials with a high tolerance to radiation fields have applications in several aerospace power and satellite systems. SiC is under investigation due to its potential for such space material applications. The effects of proton irradiation on the optical properties of the material are investigated using temperature-dependant photoluminescence (PL) and the effects of proton irradiation on the electrical properties are evaluated using current-voltage measurements and constant-voltage deep level transient spectroscopy (CV-DLTS). Subsequent high-temperature thermal annealing and recovery of the irradiated material is investigated over the temperature range of 900 – 1500 °C.

Proton-induced irradiation damage is apparent in the 4H-SiC material, affecting both the optical and electrical characteristics of the devices. The radiative behavior of the nitrogen-related near band edge transitions is significantly reduced as a result of the irradiation, with partial recovery observed after high-temperature thermal annealing at 1500 °C. A deeper trapping complex ( $E_C - E_T \cong 380$  meV) is detected as a result of irradiation and shows signs of activation due to thermal annealing. Previous research investigating ion-implantation in 4H-SiC suggests that these traps are generated independent from the type of particle implantation.

Initial indications taken from I-V measurements of the Schottky diodes reveal that proton irradiation followed by thermal annealing at 900 °C may, in fact, enhance the

rectifying device characteristics. Increasing the anneal temperature ( $T_A = 1300\text{ }^{\circ}\text{C}$ ) causes the device to fail entirely. Further annealing of the irradiated 4H-SiC at  $1500\text{ }^{\circ}\text{C}$  demonstrates recovery of the rectifying behavior of the material.

Significant levels of deep level donor traps are observed, induced by irradiation in n-type material. Three detectable defect pairs emerge with energy levels ranging from  $570 - 730\text{ meV}$  below the conduction band. The trap parameters were determined using a set of iterative curve-fitting algorithms programmed in ORIGIN<sup>®</sup> 6.1. Upon high-temperature thermal annealing of the material, the trap center pairs showed relatively little change in the energy levels and capture cross-sections while the density of traps decrease as temperatures increase. Full recovery of the material characteristics is not apparent after annealing at  $1500\text{ }^{\circ}\text{C}$ .

# **CHARACTERIZATION OF THE OPTICAL AND ELECTRICAL PROPERTIES OF PROTON-IRRADIATED 4H-SILICON CARBIDE**

## **Chapter I : Overview of Silicon Carbide Material**

### **Introduction**

There is considerable interest in developing opto-electronics capable of operating over a higher temperature range (greater than 200 °C) and with a higher tolerance against ionizing radiation than currently available. Several wide bandgap materials, such as silicon carbide (SiC) and gallium nitride (GaN), possess the optical and electrical properties necessary for constructing devices that operate in these hostile environments. The applications for such materials extend over a wide range of power and control systems, such as higher voltage/switching power MOSFETS and rectifying diodes for electric power distribution, and more powerful microwave electronics for radar and communications.

The applications for military air and space systems are equally apparent. Materials which can function efficiently at high-temperature and in high radiation fields possess the potential for integration into: 1) military surveillance and combat aircraft; 2) defense electronics and systems; 3) information systems; 4) precision weapons; 5) space systems; and 6) military aerospace structures. These materials are suitable for use in both the sensors and control systems of future cleaner-burning, more fuel-efficient

jet engines as well as in space power systems and electronic subsystems. Integration of these wide bandgap materials will provide not only superior high-voltage, high-temperature, and high-frequency switching (as compared to current materials) but also other beneficial optical and electrical properties such as increased thermal conductivity and increased tolerance to radiation damage. For space applications, these qualities may help to reduce both the size and weight of satellite systems by reducing or eliminating the need for on-board shielding and radiator equipment. A worldwide investigation into the development of wide bandgap semiconductors for use in these types of systems is ongoing [Lebedev, Neudeck (2001), Scott, Storasta].

SiC is a wide bandgap semiconductor material capable of functioning under high-temperature, high-power and high-frequency conditions, making it a candidate for a variety of electronic devices and applications. Present-day commercial satellites require thermal radiators to dissipate heat generated by the spacecraft's functional electronics. These electronics, currently based on silicon or gallium arsenide semiconductors, would fail if they were not properly cooled by the spacecraft's thermal radiators [Neudeck, 2001]. This necessitates the use of long wire runs between the sheltered electronics and the hot-area sensors and controls, or the fuel-cooling of the electronics and sensors located in high-temperature areas. Both of these low-temperature electronics approaches suffer from serious drawbacks, as the wire runs add a substantial amount of weight while fuel cooling reduces aircraft fuel efficiency, and both negatively impact aircraft reliability.

SiC electronics and sensors that function mounted in hot engine and aero surface areas of an aircraft or on satellite systems, would enable substantial weight savings, or at

least allow greater functionality (i.e., more transponders in a communications satellite) by utilizing the space and weight formerly occupied by the thermal management system [Neudeck, 2001]. Furthermore, SiC electronic devices have been shown to be less susceptible to radiation damage than correspondingly rated silicon devices. Therefore, SiC electronics could also reduce the size and weight of shielding normally used to protect spacecraft electronic components from space radiation.

### **Purpose of Research**

Satellite systems are subject to a variety of penetrating radiations. When it comes to designing space electronics, the sensitivity of the material to high-temperature and ionizing radiation is important for estimating system lifetime and requisite shielding requirements. Messenger lists the prevailing types and sources of penetrating radiation of importance, which consist of:

- 1) Solar cosmic rays, consisting chiefly of energetic protons whose energy spectrum extends beyond 100 MeV during solar flares;
- 2) Magnetically trapped protons (energies up to 40 MeV) and electrons (several keV to a few MeV) confined in the Van Allen belts about the Earth due to the interaction of the Earth's magnetic field with solar winds and;
- 3) Galactic cosmic rays, which are chiefly protons and heavy ions whose energies range from about 10 MeV to 1 GeV [Messenger:711-712].

All spacecraft and satellite systems must contend with energetic heavy charged particles. Therefore, the primary goal of this research is to document the impact of low-energy proton irradiation on 4H-SiC semiconductor material to determine the material's potential for on-board satellite electronics.

In this research, the effective proton dose at the SiC epilayer surface was calculated to be  $1.5 \times 10^{14}$  particles per  $\text{cm}^2$ . (This calculation may be referenced in Chapter IV: Proton Irradiation Sequence). Figure 1 shows the distribution of trapped protons in the Earth's radiation belts with energy greater than 1 MeV [Tascione:52].

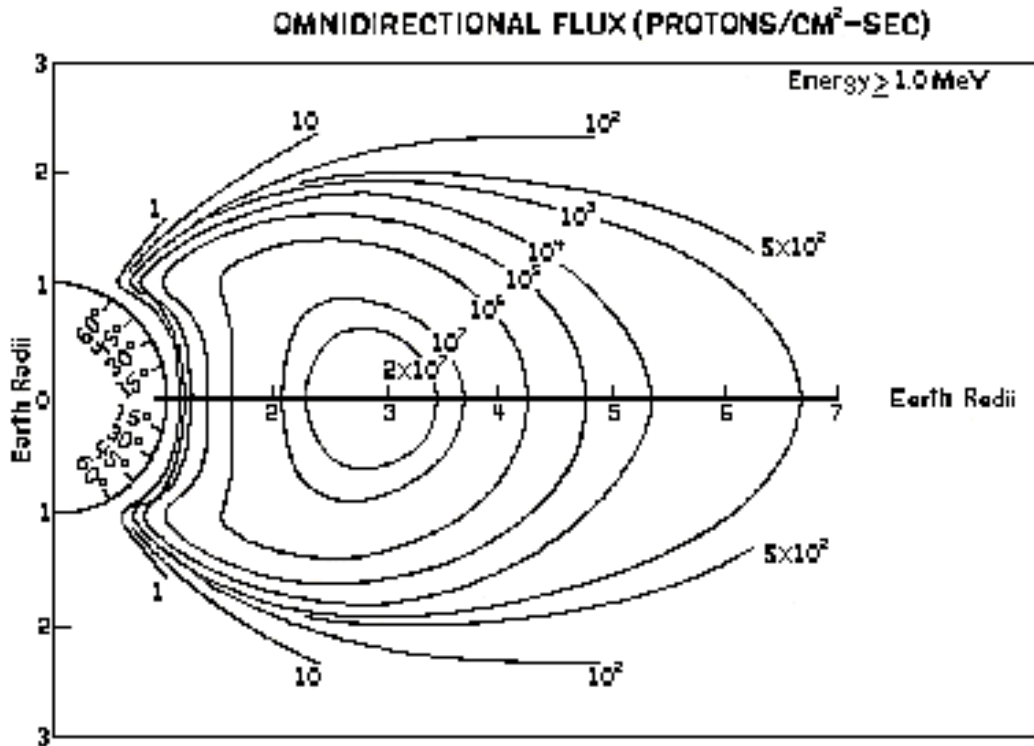


**Figure 1: Distribution of trapped protons with energy greater than 1 MeV**

Neglecting transient radiation sources (solar flare events, cosmic rays), the equivalent lifetime of a satellite, in an orbit of 4-5 Earth radii, is approximately 5 years.

The excellent optical and electrical characteristics of SiC have been known for several decades. However, only recently has the wafer growth technology been developed to where it is routine to grow high-quality, reproducible SiC material. Unlike silicon, which has been very well characterized through years of study in growth and

device fabrication, the breakdown behavior of SiC due to ion injection or other induced-defects is not well understood and models of growth and defect generation as well as damage removal techniques are required. Characterizing the radiation tolerance and response of 4H-SiC material may lead to system designs capable of reducing current leakage and aid in developing stable device characteristics for use in several air and space-based platforms.

For this research, epitaxial 4H-SiC is irradiated with 2 MeV protons to evaluate the dislocation damage effects on the optical and electrical characteristics of the material. Shallow defects formed during irradiation are investigated through the use of photoluminescence spectroscopy (PL), while deep trap centers are investigated through the use of deep level transient spectroscopy (DLTS). Through the use of characteristic photon de-excitation, PL is capable of identifying defect trap energies with great precision, provided the impurities undergo radiative recombination. It also provides a relative measure of the concentration of such defects. Using DLTS, the concentration, trap capture cross-section, and trap energy of deep level defects may be determined by examining the transient nature of the capacitance within the depletion region of a rectifying diode subjected to a constant reverse bias. Further, changes in the material resistance and majority carrier mobility are estimated by comparing the current-voltage (I-V) characteristics of the SiC Schottky diodes. A study of the irradiated material's recovery potential through high-temperature annealing is investigated. As-grown SiC material is also annealed and investigated to evaluate intrinsic defect activation.

This research began under the auspice that the SiC material would be investigated using PL to determine changes in the radiative behavior, DLTS to evaluate the

introduction of deep centers and Hall measurements to characterize the material resistivity, carrier density, and the mobility. However, the Hall equipment necessary to conduct these experiments was not available during the research quarter. To augment the Hall data, I-V curve measurements were made to evaluate changes in the 4H-SiC material resistance as a function of irradiation damage and annealing temperature.

## **Thesis Organization**

Chapter one outlines the purpose behind conducting wide bandgap semiconductor research for space-related applications and describes the overall organization for this written document. Chapter two provides a background of the physical and material characteristics of silicon carbide material and introduces the theory and consequences of radiation damage in semiconductor material. The effects of high-temperature thermal annealing are also discussed. A summary of the theory behind the PL, I-V, and DLTS semiconductor characterization methods is presented in chapter three. In addition to an outline of the material resources, irradiation, and contact procedures of the 4H-SiC samples, chapter four describes the experimental setup for each of the characterization methods used in this research. Chapter five presents the collected data with supporting analysis of the results, and chapter six provides a concluding summary of the completed work, including proposals for follow-on research.

## **Chapter II : Silicon Carbide Material Characteristics and Damage Effects**

The purpose for this chapter is to provide a brief but thorough overview of silicon carbide (SiC) material characteristics as well as model the behaviors of radiation and thermal interactions in the structured crystal lattice of semiconductor material. First, the lattice structure and bond characteristics of SiC material are discussed, highlighting the concept of polytypic growth behavior in SiC and variations in the bilayer stacking sequence to produce different optical and electrical material characteristics. Following is a summary of these material characteristics, comparing the potential of SiC to current use materials such as silicon and gallium arsenide.

The interaction of heavy charged particles through ionization and dislocation events is then discussed. The damage introduced as a result of proton irradiation causes the creation of free electron-hole carriers (short-term ionization) and the production of vacancy/interstitial point defects as a result of particle-particle interactions with lattice atoms. The effects of this damage on the optical and electrical properties of a SiC are considered and the chapter is concluded with a discussion on the effects of thermal annealing.

### **Physical and Material Characteristics of Silicon Carbide**

#### Crystalline Structure.

Silicon and carbon are both group IV elements with four valence electrons in their outermost shell. In the crystalline state, Si and C atoms form tetrahedral covalent bonds,

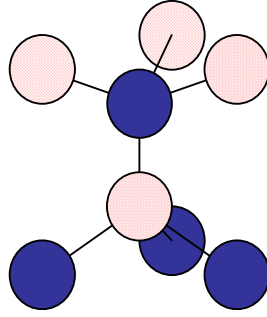


**Figure 2: SiC tetrahedral covalent bond structure**

illustrated in Figure 2, which results in a very strong stable bond structure. This molecule can form either a zincblende or a wurtzite crystal lattice structure, depending on the stacking sequence of the SiC bilayers, and the lattice stacking of SiC can take on a several stacking sequences, including cubic, hexagonal, or rhombohedral.

Each bilayer of SiC forms an equilateral triangular grid [Fig. 3(a)] such that the next bilayer must be offset in order to place its molecules over half the centers of the triangles of the previous bilayer, forming the most stable crystal structure. After the second bilayer is grown, the third bilayer may position itself in one of two ways. It may situate again to the right, offsetting a second time relative to the first bilayer in the crystal structure as depicted in Figure 3(b), or it may position itself to the left, thus placing itself directly over the first bilayer position, reference Figure 3(c).

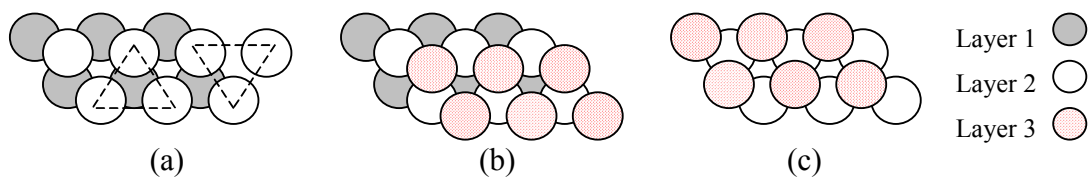


**Figure 3: (a) Triangular grid structure of a SiC bilayer (b) ABCABC SiC crystal lattice structure (c) ABAB SiC crystal lattice structure (All as viewed along the c-axis)**

Silicon carbide occurs in many different crystal structures (stacking sequences) called polytypes, with each crystal structure having its own unique electrical and optical properties. The various SiC polytypes are identical in the close-packed plane (basal) dimensions but differ in the normal dimension (c-axis). The bilayer stacking order classifies the exact crystalline polytype. A purely zincblende (diamond) structure grows in a three bilayer (ABC) repeated stacking sequence, illustrated in Figure 3(b). A purely wurtzite structure grows in a dual bilayer (AB) repeated stacking sequence, illustrated in Figure 3(c).

There are over two hundred known polytypes of SiC. However, based on their desirable optical and electrical properties, the most important polytypes for optoelectronics are 3C-, 4H-, and 6H-SiC. The Ramsdell notation is used to differentiate between the various material polytypes. For the purely cubic structure illustrated in Figure 4(a), the notation 3C-SiC is given where the number 3 refers to the number of bilayers found in the smallest repeating SiC unit, whereas the letter C stands for the overall cubic crystal symmetry [Davis:4]. Likewise for 2H-SiC [Fig. 4(b)], the overall crystal symmetry is purely hexagonal with two bilayers forming the smallest repeating SiC unit. Each lattice site has either a cubic (labeled k) or hexagonal (labeled h) configuration.

All other polytypes are a mixture of the cubic and hexagonal bonding structures. 4H-SiC takes on a quasi-hexagonal crystal structure, considered as two interpenetrating hexagonal close-packed lattices, where one lattice consists entirely of silicon atoms and the other entirely of carbon atoms [Sze:9-10]. The crystal symmetry is composed equally of one cubic and one hexagonal inequivalent site [Fig. 4(c)]. The existence of these

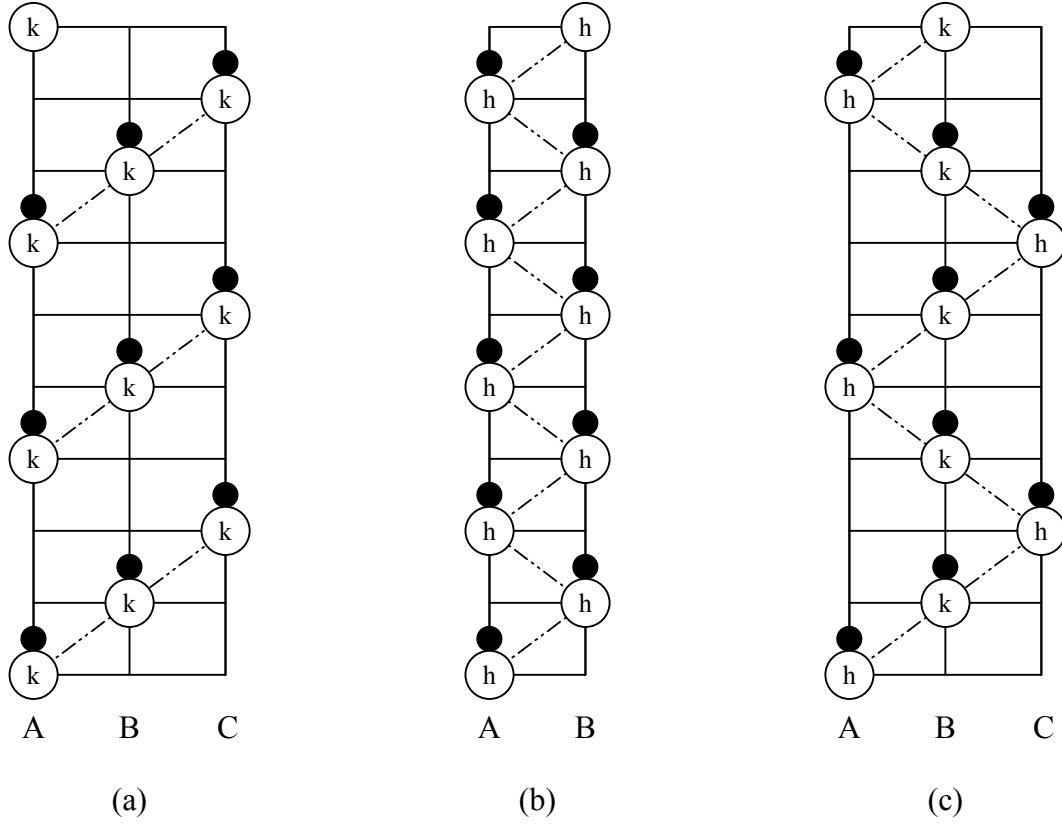


**Figure 4: (a) Pure zincblende (3C-SiC) crystal symmetry (b) Pure wurtzite (2H-SiC) crystal symmetry (c) Quasi-hexagonal (4H-SiC) crystal bonding structure**

inequivalent sites provides for the pairing of defects found in 4H-SiC, as will be discussed further in the analysis given in chapter five.

#### Electrical and Optical Properties.

The performance of a solid-state device is controlled by four major elements:

- 1) the material energy bandgap; 2) the intrinsic carrier concentration (or doping level);
  - 3) the electron-hole effective masses, and; 4) the carrier mobility [Dunn:7].
- Table 1 provides an outline of the material characteristics of SiC as it compares with silicon and

gallium arsenide semiconductor materials [Cree, Neudeck (1995), Vichare]. The bandgap energies and the electron/hole mobilities listed are for room temperature.

**Table 1: Electrical and optical characteristics of various semiconductor materials**

<b>Material / Property</b>	<b>Si</b>	<b>GaAs</b>	<b>3C-SiC</b>	<b>4H-SiC</b>	<b>6H-SiC</b>
Bandgap (eV)	~1.1	~1.4	~2.3	~3.3	~3.0
Max. Op. T (K)	~600	~760	1200	1740	1580
e <sup>-</sup> Mobility (cm <sup>2</sup> /V s)	1450	8500	1000	720	600
hole Mobility (cm <sup>2</sup> /V s)	450	400	60	60	60
Breakdown V (10 <sup>6</sup> V/cm)	0.3	0.4	4	4	4
Th. Cond. (W/cm K)	1.5	0.5	5.0	4.9	4.9
Dielectric Constant	11.9	12.9	9.7	9.7	9.7
e <sup>-</sup> Sat. Vel. (cm/s)	1.0x10 <sup>7</sup>	8.0x10 <sup>6</sup>	2.5x10 <sup>7</sup>	2.2x10 <sup>7</sup>	2.0x10 <sup>7</sup>

With a large bandgap approximately equal to 3.3 eV, 4H-SiC does not show a significant increase in intrinsic carrier concentrations, rendering 4H-SiC relatively insensitive to current/voltage fluctuations, even under high-temperature system conditions. Due to the larger breakdown voltage of such wide bandgap materials, devices fabricated from SiC operate more efficiently at higher voltages as compared to other materials. In addition, SiC is a better thermal conductor than current use semiconductor materials, allowing for: 1) greater heat dissipation (reducing the need for cooling system design integration) and; 2) stable operation at higher temperatures. Furthermore, SiC's higher electron saturation drift velocity allows for an increase in frequency switching capability and a decrease in power loss during circuit switching, as compared to current semiconductor devices made of silicon or gallium arsenide [Vichare:6-7]. These properties aid in reducing the power requirement of the device and decreasing heat production.

## **Effects of Heavy-Charged Particle Radiation**

Silicon carbide is regarded as a potential material for radiation-resistant devices. Therefore, a knowledge of the structure, energy levels, and annealing behavior of radiation-induced defects in SiC is extremely important. The proper operation of any semiconductor device depends on the near perfection of the crystalline lattice to prevent defects that can trap charge carriers. The disruptive effects of penetrating radiation however, ensure that some damage to the lattice will take place. The influence of heavy-particle radiation on semiconductor materials gives rise to a wide range of active centers, producing vacancies, interstitials, and disordered regions. These changes can lead to the degradation of the optical and electrical characteristics of these wide bandgap materials.

### Heavy Charged Particle Interactions.

Heavy charged particles, such as protons, interact with matter primarily through coulombic forces between their positive charge and the negative charge of the atomic electrons within the material atoms [Knoll:31]. Upon entering any absorbing medium, the charged particle immediately interacts with many electrons, which results in either: 1) excitation of the electron to a higher orbit or; 2) complete removal of the electron (ionization). With ionization comes the production of electron-hole pairs. Most often, these pairs recombine into a neutral state, however, in some cases, the generation of free carriers results. Depending on the state of the device during irradiation (whether an electric field is established), these charged carriers can travel through the component causing physical damage (via excess heating or arcing) as well as electrical transients that

affect the capacitance behavior and current leakage. The level of damage depends both on the incident proton flux as well as the energy of the impinging particles. In logic devices, this can lead to bit-flipping and the corruption of data and executable code.

Due to the relative mass of the proton, it is also capable of producing dislocation damage of lattice atoms in the same manner as neutrons, although the extent of the material interaction (energy transfer) is dominated by ionization. Damage caused by direct collisions of high-energy particles may produce either: 1) elastic scattering of the neutral atom from within the lattice structure or; 2) inelastic scattering with subsequent de-excitation of the atom in the form of ionizing gamma radiation. Elastic scattering, where the energy transferred from the impinging particle is great enough to mobilize the lattice atoms, can produce defects such as interstitial and vacancy centers. As a proton collides with the nucleus of a host atom, it creates what is sometimes called a primary knock-on atom (pka), leaving a point defect or vacancy behind [Ingram]. This type of defect is also commonly known as a Frenkel defect. Assuming enough energy has been transferred in the collision, the pka proceeds to cause further damage in the vicinity of the first dislocation, producing vacancy-interstitial pairs which may then annihilate between themselves or remain as defects. For SiC, it has been calculated that the minimum energy required for dislocation is approximately 40 eV.

#### Damaging Mechanism.

The damage of interest for this research was dislocation damage (damage as a result of kinetic displacement). Due to the charged nature of the irradiating protons, there will be ionization and free carrier injection, however the lifetime of these generated free

carriers may be assumed to be relatively short and that total recombination occurs almost immediately after the samples are removed from the proton beam. To measure ionization damage of this type, an in-situ data collection system would be required and was not considered for this study. Conversely, long-term dislocation damage may be apparent even after the sample is removed from the proton flux. At room temperature, vacancy-interstitial pairs in SiC introduced by the proton irradiation will not diffuse or recover quickly, allowing the material behavior to be studied over the research period without concern of the material annealing over time. The optical and electrical characteristics may then be investigated as a function of recovery due to high-temperature annealing effects.

After the damage was produced, an analysis of the defects was conducted using photoluminescence (PL), current-voltage (I-V), and deep level transient spectroscopy (DLTS) methods. The material characteristics of interest include changes in the material resistance, the emergence of shallow and deep trap energies within the bandgap, and their associated densities and capture cross-sections. Changes in the material resistance and carrier mobility are assessed by means of I-V behavior measurements, a direct measurement of the shallow energy levels is accomplished through the use of PL spectroscopy, and deep level trap parameters (trap densities, energy levels, and capture cross-sections) are extracted from the transient capacitance measurements of CV-DLTS.

### **Effects of Damage on the Material Characteristics**

The most common type of radiation-induced defect is the Frenkel defect, produced by the displacement of an atom from its normal lattice site. The vacancy left behind, together with the original atom now at an interstitial position, constitutes a

trapping site for normal charge carriers [Knoll:371-372]. With the introduction of radiation-induced defects, the lattice structure becomes more disordered and the flow of free carriers through the material is impeded. As a result, the resistivity of the material increases with a corresponding decrease in the majority/minority carrier mobilities and/or an increase in the electron/hole effective mass. These effects cause increased device heating leading to power efficiency losses. In addition, the switching frequency of a device is decreased as a result of the loss of carrier response capabilities. As the number of trapping centers increase: 1) the probability of capturing a free carrier increases and thus, the carrier lifetime is reduced and; 2) the device breakdown is decreased.

Depending on the type of material (n-type or p-type) and the behavior of the induced defect (donor or acceptor), the material may become compensated. Compensation in the semiconductor material reduces the effective dopant concentration, changing the physical properties of the SiC. For instance, if irradiating with heavy charged particles causes the effective dopant levels in n-type SiC Schottky diodes to become compensated (decreasing the effective concentration of free electrons available for conduction), the material characteristics may change sufficiently to cause the rectifying contact to exhibit ohmic behavior, introducing free-carrier injection at the contact surface, instead of the formation of a depletion region.

It is the desire of this research to establish the threshold limits of SiC to radiation damage, where the optical and electrical device characteristics begin to show signs of degradation as a function of proton irradiation as well as the level of recovery required to augment or eliminate the induced damage characteristics.

## Effects of High-Temperature Annealing

An additional goal of this research is to determine the effects of high-temperature annealing ( $T_A$ ) on proton-irradiated SiC samples. The results may then be used for comparison of the defect's annealing behavior to other thermal-anneal studied defects and possibly for developing damage recovery methods for space-based SiC devices. As a result of the formation of a damage region and defect clusters due to the proton irradiation, the carrier mobility and lifetime in semiconductor materials are severely degraded. Thermal annealing adds energy to the lattice structure, allowing mobilization of trapping centers and other defects that can, in turn, recombine to form shallow defects, migrate out of the active region, or become fixed at a lattice site.

At extremely high temperatures, the crystal may even begin to disassociate and recrystallize upon cooling. For bulk or uniformly doped material, this may not cause a problem but it becomes an issue when the device requires the use of a highly defined geometric region of extrinsically doped material. As the temperature increases, diffusion of atoms throughout the lattice structure will occur and the device characteristics could be permanently altered. Whether there exists an annealing temperature where the damage recovery is maximized without affecting the original device characteristics is under investigation. Effective diffusion in SiC material requires temperatures greater than 1800 °C [Harris:153], and the sublimation temperature of SiC is greater than 2100 °C [Scott:II-6]. Since the thermal annealing of the irradiated material in this study does not exceed 1500 °C, carrier diffusion and crystal disassociation of the sample material are not a concern.

If a suitable annealing mechanism may be incorporated into the design of space/satellite equipment, the longevity and efficiency of the system may be enhanced. On the other hand, in the event that in-situ annealing of space-bound SiC devices is not possible, the data recorded here will serve as a stepping-off point towards the development and integration of alternative system designs.

### **Chapter III : Methods of Semiconductor Characterization**

The following chapter provides a brief summary of the theory behind the various semiconductor characterization methods used in this research. The technique of photoluminescence (PL) spectroscopy is discussed first, outlining its method for shallow level characterization, the types of transitions that may be classified, and the nomenclature established for describing important structure in the PL spectra. Following is a discussion on the method of current-voltage (I-V) characterization for evaluating the rectifying behavior of SiC Schottky diodes. A summary on the technique of constant voltage deep level transient spectroscopy (CV-DLTS) concludes the chapter, describing the formation of a space charged region (similar in theory to a parallel plate capacitor), developing the rate window concept (boxcar DLTS) for measuring changes in capacitance, and illustrating the relationship between the capacitance as a function of temperature with the defect-associated trap parameters.

#### **Photoluminescence Spectroscopy**

The technique of PL excitation may be used as a fast and nondestructive characterization method for epitaxially grown 4H-SiC. This method consists of impinging relatively high frequency ( $h\nu > E_g$ ) light onto a material, exciting atomic electrons. Subsequent relaxation may result in the production of photons that are characteristic of the atom or defect site that emitted the light. The luminescent signals detected could be intrinsic crystalline defects (growth defects), dopant impurities

(introduced during growth or ion implantation), or other extrinsic defect levels (as a result of radiation or thermal effects). When bombarded with photons of energy greater than the bandgap of the material, an impurity energy level may emit characteristic photons via several different types of radiative recombination events, allowing the resultant PL spectra to then be used to determine the specific type of semiconductor defect. This interaction provides a highly sensitive, qualitative measurement of native and extrinsic impurity levels found within the SiC material bandgap.

#### Radiative Transitions.

When a semiconductor absorbs a photon of energy greater than the bandgap, an electron is excited from the valence band into the conduction band leaving behind a hole. When the electron returns to its original state, it may do so through radiative (release of a photon) or non-radiative (no photon production) recombinations. PL is only capable of detecting radiative transitions within the bandgap. When the electron and hole recombine through radiative recombination, a photon is emitted and the energy of the emitted photon is dependent on the change in energy state of the electron-crystal system. Because SiC is an indirect bandgap semiconductor, photon emission requires the aid of a phonon (energy in the form of lattice vibrations) to conserve momentum within the lattice structure [Davis:12]. This will become important in the analysis of the PL spectra discussed in chapter five.

With the introduction of impurities in semiconductor material comes the introduction of discrete energy levels within a semiconductor's forbidden energy gap. Shallow donor levels are defined as levels just below the conduction band, whereas,

shallow acceptor levels are defined as levels just above the valence band. These donor or acceptor level traps can act as recombination centers for transitions within the bandgap. By studying the nature of these trap levels, information about the impurity or defect can be resolved. Figure 5 represents the energy band diagram of a semiconductor, illustrating the most common radiative transitions. The conduction band ( $E_C$ ), occupied by free electrons, and the valence band ( $E_V$ ), occupied by free holes, are represented in addition to donor ( $E_D$ ) and acceptor ( $E_A$ ) trapping centers within the forbidden gap.

The first transitions described here are band-to-band or direct recombinations [Fig. 5(a)], which dominate at room temperature and may be used to estimate the material bandgap energy ( $E_g$ ). For indirect semiconductors, such as SiC, a band-to-band recombination process is unlikely because the electrons at the bottom of the conduction band have a nonzero crystal momentum with respect to the holes at the top of the valence band

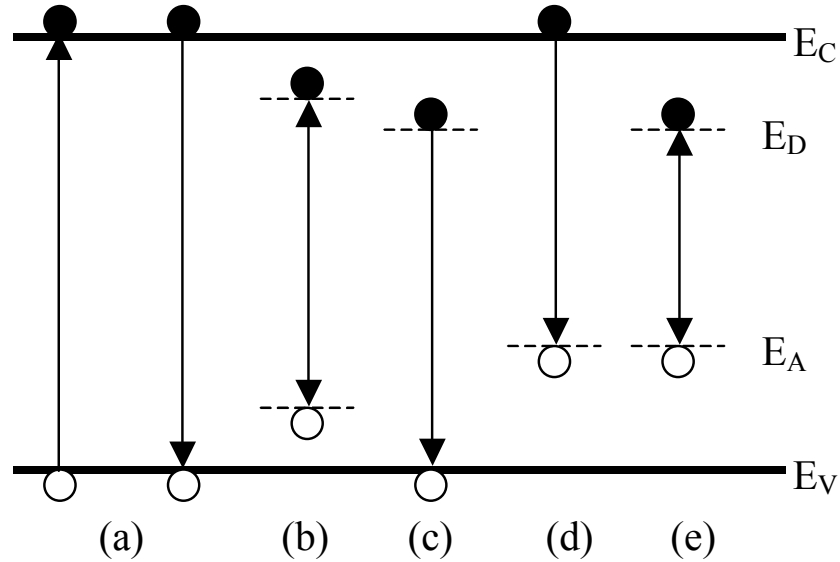


**Figure 5: Most common radiative transitions observable with photoluminescence**

band. A direct transition that conserves both energy and momentum is not possible without a simultaneous lattice interaction (phonon emission) [Sze:48].

A different type of transition, excitonic recombination, can occur following the generation of an electron-hole pair [Fig. 5(b)]. Coulombic attraction leads to the formation of an excited state in which an electron and the hole remain bound to each other in a hydrogen-like state, referred to as a free exciton [Schroeder:624]. The couple may move freely throughout the crystal, but the electron and hole are bound and move together.

A free hole may combine with a neutral donor [Fig. 5(c)] or an electron may combine with a neutral acceptor [Fig. 5(d)], via single-level recombination, to form a bound exciton. Because only one hole/electron can occupy a given center, the rate of carrier capture is proportional to the concentration of centers. Conversely, the carrier emission rate is proportional to the number of centers occupied. At thermal equilibrium the capture and emission rates must be equal. It stands to reason that an electron trap close to the conduction band or a hole trap close to the valance band has a higher capture/emission probability than those centers located further away from the band edge.

The last transition is that of a multi-level donor-acceptor recombination between the electron of a neutral donor and the hole of a neutral acceptor positioned within the material bandgap, illustrated in Figure 5(e). Intuitively, these transitions involve chemical impurities and/or physical defects in the material, which introduce trapping centers within the forbidden bandgap.

### PL Spectrum Nomenclature.

The spectrum depicted in Figure 6 illustrates a PL spectrum of the n-type (nitrogen-doped) as-grown 4H-SiC material used in this study. The term “near band edge” refers to transitions close to the bandgap energy,  $E_g$ . The near band edge peak structure is located at the right edge of each PL spectra presented. Luminescent peaks to the left of the band edge (between  $\sim 3.0$  and  $3.25$  eV) represent shallow trap (and associated phonon replica) behaviors located deeper in the bandgap. An absolute measure of the density of traps cannot be taken from the peak intensity, since the intensity is dependent on several experimental factors including: 1) how well the PL

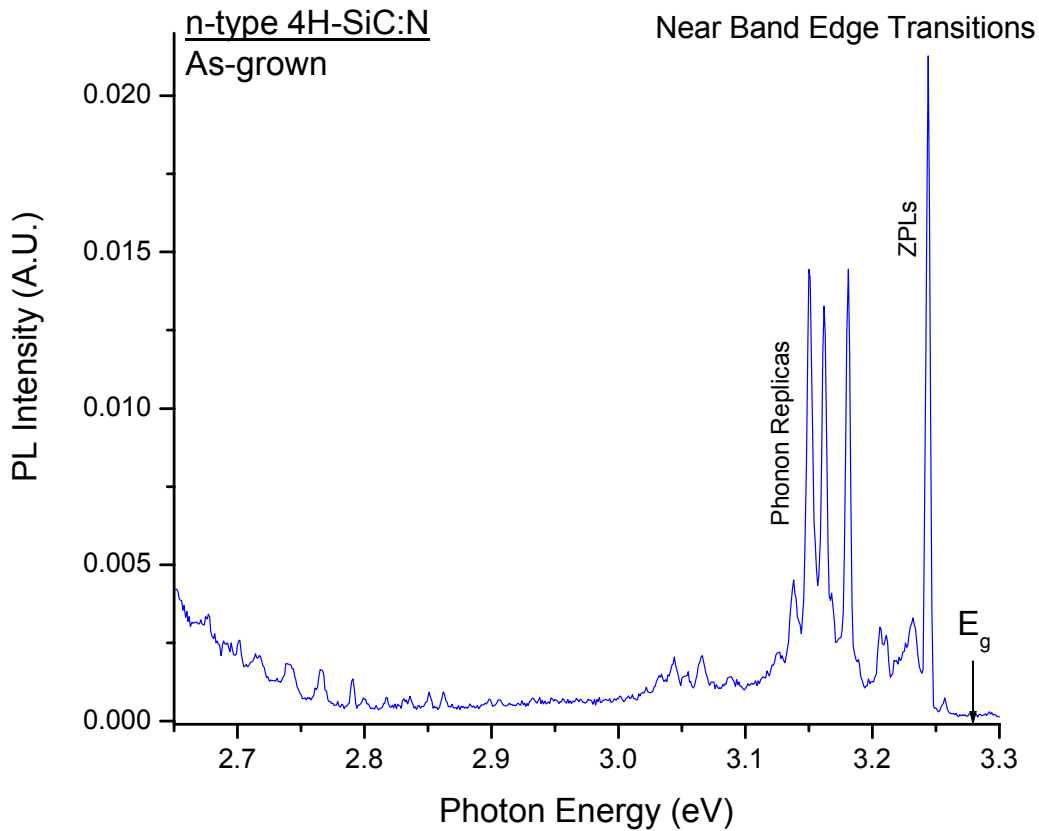


**Figure 6: Photoluminescence spectra of as-grown n-type (nitrogen-doped) 4H-SiC**

system laser optics are aligned; 2) the system laser power; 3) the orientation of the sample relative to the incoming beam and; 4) the optical quality of the samples themselves. Therefore, only relative changes in the peak structure as a result of thermal quenching, irradiation, and/or high-temperature annealing are discussed in this document.

The peak energy position (x-axis) characterizes the trap energy (and phonon energy spacing) and the relative peak height (y-axis) is dependant on the trap density and/or capture cross-section as well as the probability of escaping the material without re-absorption. The photon emission (trap energy) may be expressed in units of wavelength or energy. The equivalence is proportional to Planck's constant in the form:

$$E = \frac{hc}{\lambda} \quad (3-1)$$

where h is Planck's constant ( $6.626 \times 10^{-34}$  J·s), and c is the speed of light in a vacuum.

Upon proton irradiation, additional photon peaks, which are characteristic of induced damage centers, may become present. A comparison of pre-irradiated data with measured data after irradiation is used to determine the defect energy and the relative concentration introduced due to proton bombardment. One of the many benefits of this characterization technique is that it is non-destructive and requires no metal contact processing of the samples.

## I-V Diode Characterization

Current-voltage (I-V) measurements may be used to determine the rectifying properties of a diode. A voltage applied to a Schottky junction disturbs the balance between the steady state diffusion and drift currents of electrons and holes in the depletion region. Under forward bias, the applied voltage reduces the electrostatic potential across the depletion region, reducing the drift currents and causing minority carrier injection across the barrier. Under reverse bias, the applied voltage increases the electrostatic potential across the depletion region, greatly reducing the diffusion currents which results in a small reverse current [Sze:87-88]. The thermionic current-voltage expression of a Schottky barrier diode is given by Equation 3-2 [Schroder:205].

$$I = I_s \left[ e^{\left( \frac{q(V - I r_s)}{nkT} \right)} - 1 \right] \quad [\text{A}] \quad (3-2)$$

where  $I_s$  is the saturation current,  $r_s$  is the device equivalent series resistance and,  $n$  is the barrier ideality factor. If both  $I_s$  and  $n$  are assumed constant, then the I-V relationship can be related to the material resistance.

The I-V curve measurements functioned both as a diagnostic tool to determine the quality of the device contacts as well as a characterization technique for the evaluation of the diode properties. The system was first used during the contact fabrication phase of the research as a method for confirming whether an ohmic contact was established on the SiC material. The process took several tries to verify the correct metal and required anneal temperature. After this segment of the fabrication process was complete, the I-V

probe station was again utilized to verify the rectifying behavior of the Schottky contacts. The relationship between the change in material resistance as a function of irradiation and thermal anneal and the rectifying behavior of the SiC device is then used as a measure of the device quality.

### **Deep Level Transient Spectroscopy**

PL may not be adequate for characterizing deeper-level defects due to a decreased probability of excitation without re-absorption at lower energy levels. It is also unsuitable for characterizing any non-radiative transitions. For this work, deep level transient spectroscopy (DLTS) is preferred. Capacitance transient techniques are powerful tools for the characterization of radiation-induced active deep levels in semiconductors, providing insight into important parameters such as ionization energies, defect concentrations, and capture cross-sections and their thermal behavior. The technique of constant-voltage DLTS (CV-DLTS) makes use of the temperature dependence of the transient capacitance due to a filling and subsequent thermal detrapping of defect centers located inside an induced space charge region (SCR) while holding the applied voltage at a constant level. By measuring the transient pulse height, it becomes possible to determine the effective defect density. By measuring the transient capacitance behavior over a range of temperatures, it becomes possible to determine the associated trap activation energy and capture cross-section.

In DLTS, the material being studied is fabricated into a junction device such that a reverse bias may be placed across the device in order to generate a depletion region.

The depletion region is a space charge region formed by the ionized fixed lattice ions at the interface due to free carrier drift currents. Deep traps within the material bandgap contribute to the free carrier density and thus affect any type of capacitance measurement. Their influence is based on the nature and concentration of the traps, the trap energy, and the trapping efficiency of the capacitance method. In order to take advantage of this influence, each semiconductor sample is processed into a one-sided rectifying diode where the SCR may act as a capacitor, depleting only into the SiC epilayer, and the applied bias across the sample becomes the independent control variable ( $C=f(V)$ ).

#### Constant-Voltage DLTS.

Consider a Schottky diode that had been reverse-biased sufficiently long that all majority carriers have been emitted from the SCR (steady state). When the diode is pulsed from reverse bias to a zero or forward bias, electrons rush into the SCR to be captured by unoccupied trap centers. In such a transient measurement, it is the time-varying depletion width,  $W$ , that is detected as a time-varying capacitance, [Schroder:276]:

$$C = A \sqrt{\frac{qK_s\epsilon_0(N_D - N_A)}{2(V_{bi} - V_{rev})}} \sqrt{1 - \frac{N_T}{(N_D - N_A)}} = C_0 \sqrt{1 - \frac{N_T}{(N_D - N_A)}} \quad [F] \quad (3-3)$$

where  $C_0$  is the capacitance of a device with no deep-level impurities at reverse bias,  $V_{rev}$ , the quantity  $(N_D - N_A)$  is the effective doping density, and  $N_T$  is the steady-state trap density in the reverse-biased SCR, given by Equation 3-4 [Schroder:274].

$$N_T = \frac{e_p}{e_n + e_p} (N_D - N_A) \quad [\text{cm}^{-3}] \quad (3-4)$$

The variables  $e_n$  and  $e_p$  represent the emission rate constants for the majority and minority carriers respectively.

For the derivation of Equation 3-3, several assumptions, known collectively as the depletion approximation, are made, allowing the semiconductor to be divided into two distinct regions [Blood:235]. The first is a region of total depletion of majority carriers existing in the SCR. The second is a region beyond the depletion depth,  $W$ , where perfect charge neutrality exists in the bulk. The boundary between the two regions is sharp and defines the depletion depth,  $W$ . In general, this is a reasonably good approximation for materials where the SCR is reverse biased and where the substrate is uniformly doped [Schroder:66], as is the case in this research.

For the most common use of transient capacitance measurements, the deep-level impurity concentrations are relatively small, forming only a small fraction of the SCR [Schroder:276]. Hence, one is looking for trace amounts of impurities, allowing Eqn 3-3 to be simplified using a first-order Taylor expansion [Schroder:276]. [Eqn 3-5]

$$C \approx C_0 \left( 1 - \frac{N_T}{2(N_D - N_A)} \right) \quad [\text{F}] \quad (3-5)$$

Equation 3-5 represents the *steady-state* capacitance in the depletion region due to a constant reverse-bias,  $V_{\text{rev}}$ . Following a reverse bias pulse, majority carriers are emitted exponentially as a function of time [Schroder:290] with the corresponding transient capacitance:

$$C(t) = C_0 \left( 1 - \frac{N_T(0)}{2(N_D - N_A)} \right) e^{\left( \frac{-t}{\tau_e} \right)} \quad [\text{F}] \quad (3-6)$$

where  $\tau_e$  is the majority carrier emission time constant as a function of temperature and is given by Schroder [Schroder:290].

$$\tau_e = \frac{1}{\gamma_n \sigma_T T^2} e^{\left[ \frac{(E_C - E_T)}{kT} \right]} \quad [\text{s}] \quad (3-7)$$

The variable  $\gamma_n$  is a material coefficient dependent on the material type [Schroder:280]. The capture cross-section,  $\sigma_T$ , is therefore characterized through the measurement of  $\tau_e$ .

Recall, the SCR is widest and the capacitance is lowest immediately after the device is reverse-biased. As majority carriers are exponentially emitted from the traps, the depletion width,  $W$ , decreases and the capacitance increases until the steady state has returned. The capacitance increases with time for majority carrier emission regardless of whether the substrate is n- or p-type and whether the deep-level impurities are donors or acceptors [Schroder:277].

### Boxcar DLTS.

Suppose that the C-t waveforms are gated at times  $t_1$  and  $t_2$  and that the capacitance at  $t_2$  is subtracted from the capacitance at  $t_1$ , as shown in Equation 3-8.

$$\delta C = C(t_1) - C(t_2) \quad (3-8)$$

Such a difference signal is a standard output feature of a double boxcar instrument [Schroder:290-291]. The temperature is slowly scanned while the device is repetitively pulsed between zero and reverse bias. There is very little difference between the capacitance values at the two sampling times for very slow or for very fast transients ( $\delta C \approx 0$ ), corresponding to low and high temperatures. A difference signal (change in the capacitance) is generated with a time constant, on the order of the gate separation,  $t_2 - t_1$ , and the capacitance difference passes through a maximum as a function of temperature. This is the DLTS peak depicted in Figure 7. By generating a series of C-t curves at different temperatures for a given gate setting  $t_1$  and  $t_2$ , one value for  $\tau_e$ , corresponding to a particular peak temperature, is computed.

Bringing the squared temperature term over to the left side of Equation 3-7, the emission time constant may be written in the following manner.

$$\tau_e T^2 = \frac{1}{\gamma_n \sigma_n} e^{\left[ \frac{(E_c - E_T)}{kT} \right]} \quad (3-9)$$

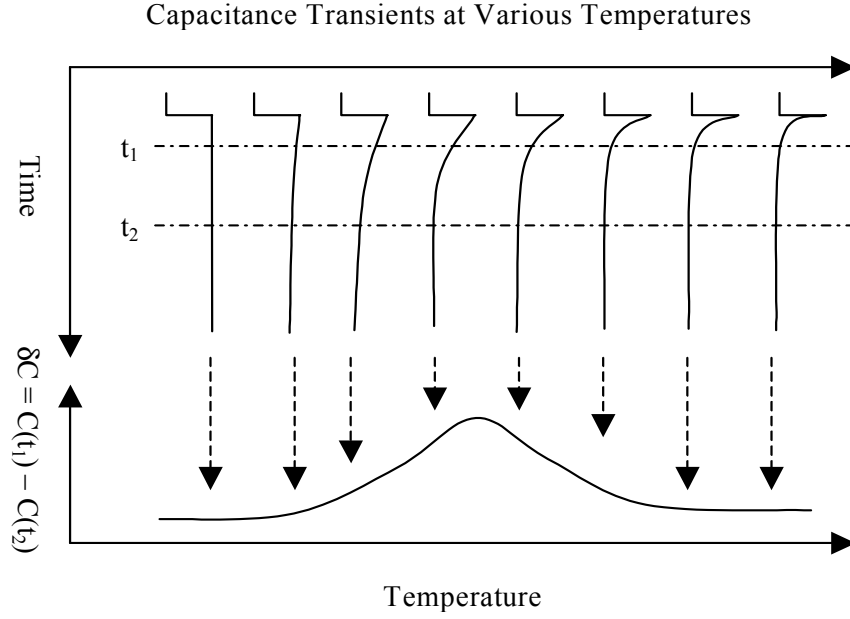


**Figure 7: Rate window concept of boxcar DLTS. A series of C-t curves, at different temperatures, for a given gate setting  $t_1$  and  $t_2$ , are analyzed to determine the characteristic emission time constant.**

A plot of  $\ln(\tau_e T^2)$  versus  $(1/kT)$  yields a straight line with a slope of  $(E_c - E_T)$ , providing the defect trap energy, and a y-intercept of  $\ln(1/\gamma_n \sigma_n)$ , which leads to the capture cross-section [Schroder:281]. Graphs that plot the natural log versus the exponent variable are known as Arrhenius plots.

The density of defects ( $N_T$ ) in the material is related to the magnitude of the  $\Delta C$  signal at the peak temperature, which can be shown to be equal to:

$$N_T \cong 2(N_D - N_A) \frac{\Delta C}{C_0} \quad [\text{cm}^{-3}] \quad (3-10)$$

for  $\delta C \ll C_0$  [Scofield:IV-8].

A single peak may be fitted using a single exponential with only three variable fitting parameters ( $N_T$ ,  $\sigma_T$ , and  $E_T$ ) by combining Equations 3-6 and 3-7:

$$C(t) = C_0 \left( 1 - \frac{N_T(0)}{2(N_D - N_A)} \right) e^{\left( \frac{-t}{\left( \frac{1}{\gamma_n \sigma_T T^2} e^{\left[ \frac{(E_C - E_T)}{kT} \right]} \right)} \right)} \quad [\text{F}] \quad (3-11)$$

However, when the peak structure is composed of multiple peaks, the model must be expressed as a sum of multiple exponential terms.

$$C(t) = C_0 - \frac{C_0}{2(N_D - N_A)} \sum N_{T,i} e^{\left[ \frac{-t_i}{(\tau_{e,i})} \right]} \quad [\text{F}] \quad (3-12)$$

Such is the case for SiC where its polytypism results in close energetic level pairs due to lattice inequivalencies.

## **Chapter IV : Material and Experimental Resources**

The purpose for chapter four is to outline the various elements that make up the experimental process taken during this research, including a description of the sample material itself, the organizational breakdown of the various sample sets within the total investigation matrix, a review of the Ohio University irradiation sequence, and the equipment involved in the characterization phase. The SiC wafers were segmented into four groups: 1) as-grown material; 2) as-grown and annealed material; 3) irradiated material and; 4) irradiated and annealed material. Each annealing group was further subdivided in to four temperature categories. The effects of proton beam current and sample orientation on the absorbed dose value are discussed and the methodology behind calculating the dose at the epilayer surface is presented. The recipe for the contact metallization processes is summarized and the chapter is concluded with a detailed description of the experimental set-ups for each of the three characterization techniques, photoluminescence (PL), I-V curve measurements, and deep level transient spectroscopy (DLTS).

### **4H-SiC Material**

#### Wafer background.

Sample preparation includes device fabrication, material irradiation and high-temperature annealing. The sample wafer set used for this research is comprised of two research-grade 4H-SiC wafers purchased from Cree Inc. Table 2 summarizes the details

for each wafer, including the wafer ID number, the growth methods used for both bulk and epitaxial growth, the dopant used in each wafer type, and the total doping density within the epitaxial surface layer (epilayer).

Only the epilayer was investigated in both wafer types. A 4H-SiC boule was grown by Cree<sup>®</sup> using seeded sublimation techniques, sliced into wafers and then polished. An epilayer (approximately 5  $\mu\text{m}$  thick) was grown by Cree<sup>®</sup> on the SiC substrate via chemical vapor deposition (CVD) growth. The respective nitrogen and aluminum dopant atoms are incorporated during the epitaxial growth sequence.

**Table 2: Cree<sup>®</sup> research-grade wafers used for this study**

Wafer ID	Substrate (Sublimation)	Epilayer (CVD)	Dopant	$(N_D - N_A) (\text{cm}^{-3})$
AG0746-03	n-type 4H	n-type 4H	N	$1.2 \times 10^{17}$
AQ0528-06	p-type 4H	p-type 4H	Al	$1.5 \times 10^{18}$

Because the epilayer is generated on a conducting SiC substrate, Schottky and ohmic contacts may be constructed on the front (epilayer surface) and back substrate respectively, instead of requiring concentric circular contacts only on the front. The first configuration is preferred because it is the simplest to model. With concentric contacts, the analysis becomes more difficult due to lateral current flow and current crowding effects at the contact edges [Schroder:143-145]. The first wafer consists of an n-type epilayer on an n-type substrate ( $10^{17} \text{ cm}^{-3}$ ). The second wafer consists of a p-type epilayer on a p-type substrate ( $10^{18} \text{ cm}^{-3}$ ).

The initial preparation of these samples represents one of the most important steps in the process of this investigation. Each wafer was inspected using a set of polarizing lenses to map large scale intrinsic defects on the surface due to wafer stressing during growth and shipping. Non-destructive verification of manufacturer's listed doping levels and material resistivity could be achieved through the use of mercury probe resistivity measurements, however the equipment for this work at AFIT was unavailable at the time of initial wafer inspection. Following inspection, the wafers were cut into 5x5 mm test samples.

#### Matrix Organization.

In order to develop a correlation between the induced damage defects and the material behavior, it was necessary to construct a baseline measurement for comparison. All the induced proton damage and thermal recovery was evaluated using relative measurements. To make these comparisons, a set of control samples, consisting only of as-grown wafer material, was processed into test devices. Table 3 was constructed in an effort to organize the number of samples required to conduct a comprehensive annealing study. As-grown samples are necessary in order to evaluate changes in the material behavior as a result of the irradiation. As-grown material is also annealed at high temperature in order to investigate the initial quality of the material and to confirm whether or not changes in the material properties are due to thermal activation of defects already present in the material. The irradiated samples were used to determine the level of damage as a result of the proton irradiation and further, the effects of subsequent high-temperature annealing. The material was annealed at four different temperature steps

ranging from 900 to 1500 °C. A minimum of two 5x5 mm samples, each consisting of 20-30 Schottky diodes, were prepared for each wafer and category except for the as-grown/annealed category, in which only one sample for each temperature step was processed. This exhausted the 4H-SiC inventory.

**Table 3: Sample matrix for comprehensive proton irradiation/anneal study**

Wafer ID	As-grown	As-grown/Annealed	Irradiated	Irradiated/Annealed
AG0746-03	2	4	2	8
AQ0528-06	2	4	2	8

### **Proton Irradiation Sequence**

Prior to Schottky diode fabrication, the samples are bombarded with 2 MeV protons to a dose of approximately  $1.5 \times 10^{14}$  particles/cm<sup>2</sup> in a Van de Graaff accelerator located at the Ohio University's Edwards Accelerator Facility [Dr. David C. Ingram, Athens OH, 45710]. Each sample is mounted onto a stainless-steel sample finger using carbon tape. Once the samples are set in the beam tube, the system is evacuated. The samples are irradiated using an overlapping swept beam and the system is brought back to atmospheric pressure before the chamber is opened for sample removal. The sample finger is grounded to prevent charge buildup on the SiC samples. (As positive charge builds on the material surface, the succeeding proton beam current would be deflected due to coulombic forces and sample irradiation would be altered or perhaps stop).

Two columns of eight samples were mounted for each implant sequence. The total aperture of the beam sweep was then 4 cm high and 1 cm wide. The beam swept

across the sample in 0.25 mm steps in the vertical direction (y-axis) and 0.5 mm steps in the horizontal direction (x-axis) [Fig. 8] and the integrated time over target is two seconds. Therefore, the cross-sectional target area,  $A_0$ , can be approximated as

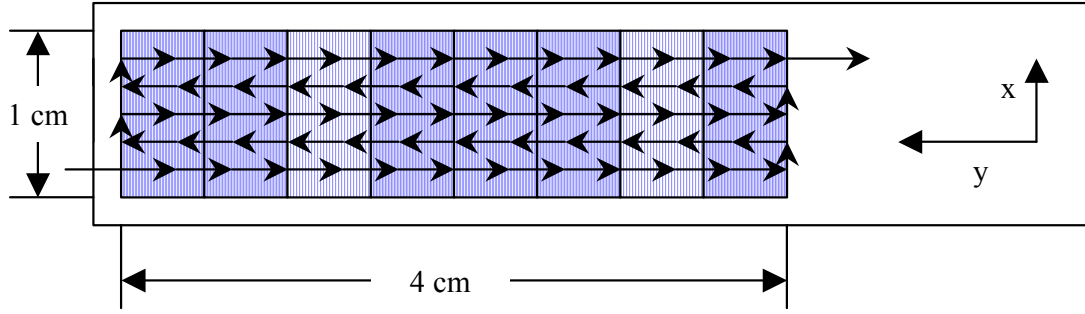


**Figure 8: 4H-SiC sample layout on the stainless steel finger. A 2 MeV proton beam is stepped across the samples to irradiate the material uniformly.**

$1.25 \times 10^{-3} \text{ cm}^2$ . As a result of target stepping across the samples, the absorbed dose may be described as the sum of a series of Gaussian curves representing the energy deposited at each location. The result is a uniform absorbed proton dose (at constant depth) across the sample face [Fig. 9(a)].

A proton beam current ( $I_b$ ) of approximately 10 nA or  $6.25 \times 10^{10}$  particles/second is stepped across the target area at an offset angle of  $45^\circ$  [Fig. 9(b)]. The samples were offset in order to increase the time of interaction of the charged particle inside the epitaxial layer, since this is the region of interest. The epilayer thickness is approximately  $5 \text{ }\mu\text{m}$ . At an angle of  $45^\circ$ , the particle's path may be described by taking the product of the thickness and the sine of the angle. As a result, the effective distance the particle travels (and deposits energy) inside the epitaxial layer is increased to approximately  $7.1 \text{ }\mu\text{m}$ .

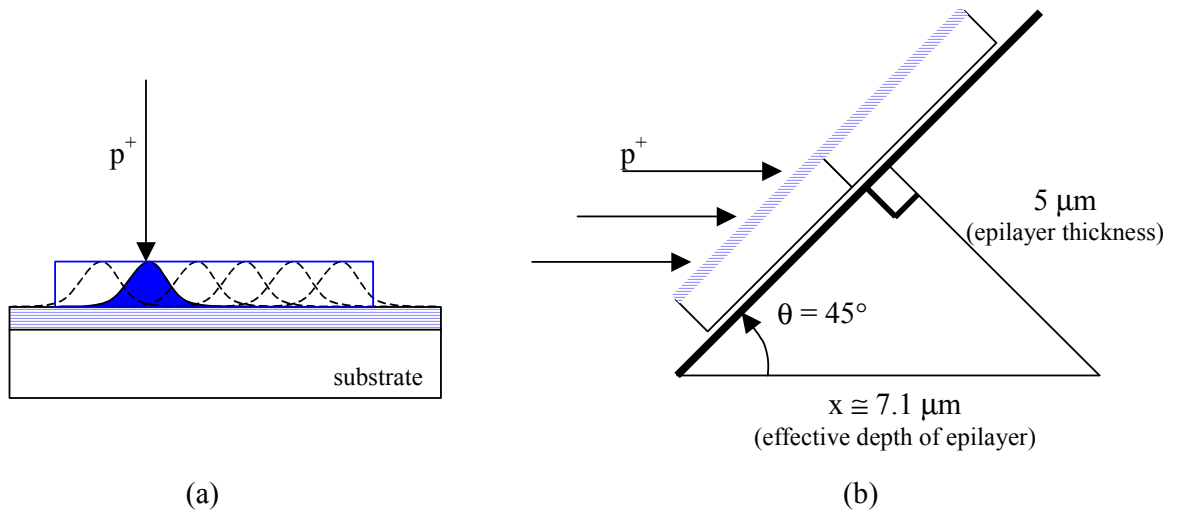


**Figure 9: (a) A series of Gaussian curves represents the 25x50 mm beam aperture as it steps across the samples to produce a uniform dose in the 4H-SiC material (b) 4H-SiC sample orientation with respect to incoming proton beam**

If the beam current ( $I_b$ ), the irradiation period ( $t$ ), and the effective target area, ( $A = A_0 \sin \theta$ ), are known, the proton fluence ( $\psi$ ) may be calculated using:

$$\psi = \frac{I_b t}{A} \quad [\text{cm}^{-2}] \quad (4-1)$$

so that the calculated dose is approximately  $1.5 \times 10^{14} \text{ cm}^{-2}$ .

### Contact Fabrication

All metal contact fabrication for Schottky diodes was performed at the Air Force Institute of Technology's (AFIT) clean room facilities. The samples were first cleaned by degreasing them using trichloroethylene (TCE) followed by a rinsing with acetone and methanol, and then dried using nitrogen gas ( $\text{N}_2$ ). Next, the samples were placed in

boiling 3:1 aqua-regia (HCl:HNO<sub>3</sub>) solution to remove any oxide layer, followed by another rinse in deionized water and N<sub>2</sub> dry. After cleaning, Ni (2000 Å) and Ti/Al (200 Å/1800 Å) backside ohmic contacts were fabricated on the n-type and p-type material, respectively. To reduce the contact resistance, the Ni contacts were then annealed for five minutes and the Ti/Al contacts were annealed for two minutes, each in a tube furnace at 900 °C under a nitrogen gas flow. Prior to Schottky metal patterning, the epilayer surface was once again cleaned using the TCE:acetone:methanol baths followed by a N<sub>2</sub> dry. Subsequently, circular Ti contacts (0.5 mm in diameter and 0.2 µm thick) were deposited on both the n and p-type material to form Schottky barrier contacts. The exact processing details involved are outlined in the Appendix.

### **High-Temperature Annealing**

Four sets of samples were annealed using AFIT and Air Force Research Laboratory (AFRL) furnace equipment. A Lindberg<sup>®</sup> BlueM tube furnace, model MiniMite, was used to anneal samples at 900 °C and 1100 °C for twenty minutes in an atmosphere of flowing nitrogen gas. The maximum furnace temperature however, could not exceed 1200 °C. Therefore, samples requiring anneal temperatures of 1300 °C and 1500 °C were taken to the Materials Directorate of AFRL and annealed in an Oxy-Gon<sup>®</sup>, model FR200, high-temperature furnace. These anneals also took place under a flowing nitrogen atmosphere. Table 4 lists the number of n- and p-type 4H-SiC samples annealed at each anneal temperature.

**Table 4: Thermal anneal study matrix**

<b>Annealing Study</b>	<b>n-type (AG0746-03)</b>		<b>p-type (AQ0528-06)</b>	
	As-grown	Irradiated	As-grown	Irradiated
0 °C	2	2	2	2
900 °C	1	2	1	2
1100 °C	1	2	1	2
1300 °C	1	2	1	2
1500 °C	1	2	1	2
<b>TOTAL</b>	16		16	

### Experimental Apparatus Set-up

#### Photoluminescence.

All photoluminescence (PL) measurements were performed at the AFIT Research Laboratory facility. A diagram describing the experimental PL set-up is presented in Figure 10. Each sample was mounted to a cold finger with rubber cement and placed into a liquid helium-cooled cryogenic dewar that was cooled to a sample temperature of 10 K. The temperature of the sample was monitored using a 330 Lakeshore<sup>®</sup> temperature controller. The measured luminescence was generated by a 275 nm Argon ion laser system operating at 600 mW. The light emitted was collected and analyzed in a Spex<sup>®</sup> model 750M  $\frac{3}{4}$  meter monochromator with an entrance and exit slit width of 400  $\mu\text{m}$ . The monochromator is equipped with a 3000 Å blaze grating with 1200 grooves/mm and the photon signals were detected by a liquid nitrogen-cooled GaAs photomultiplier tube (PMT) operating at 1800 V. The PMT analog signal was then digitized and recorded by a data acquisition system (DAS). The monochromator and PMT detector were controlled by the DAS using Spex<sup>®</sup> DataScan software.

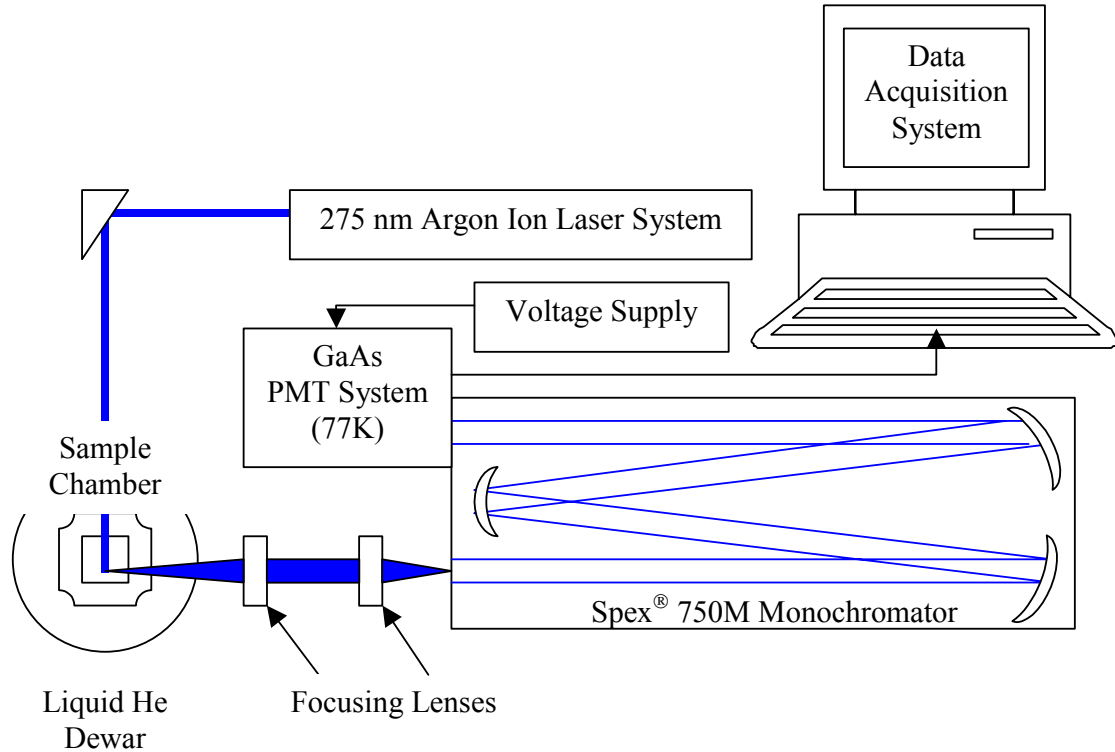


**Figure 10: Photoluminescence laboratory set-up**

#### I-V Curve Measurements.

In addition, all current-voltage measurements were conducted at the AFIT laboratories. The probe station used for making electrical contact is a Cascade Microtech® Alessi REL-6100. The tungsten electro-probes lead from the device to a Hewlett Packard, model 4155A, semiconductor parameter analyzer. This is where a current is forced through the diode, the voltage is measured, and the resultant I-V curve is plotted. The probe station makes use of a Panasonic® GP.KR222 frame-grabber video camera to provide instantaneous video of the device on the probe station and may be used to create digital picture files. The camera is positioned over a microscope with a x10 objective. The entire system is controlled by a data acquisition system.

### Deep Level Transient Spectroscopy.

All DLTS measurements were also carried out at the AFIT laboratories. An outline of the experimental set-up is illustrated in Figure 11. The sample chamber consisted of a CTI<sup>®</sup> model 22 closed-cycle cryogenic dewar. A Drytel<sup>®</sup> 31 vacuum system was used to evacuate the chamber and temperature control was achieved using a 330 Lakeshore<sup>®</sup> temperature controller. Each sample was mounted in the cold-head with the backside ohmic contact resting on an isolated conducting plate while pressure point contacts were aligned to selected diodes on the patterned Schottky surface. The leads from the plate and the point contacts connect to a SULA<sup>®</sup> Technology Deep Level Spectrometer, synchronized and triggered through a LeCroy<sup>®</sup> 9210 Pulse Generator. A LeCroy<sup>®</sup> 9410 Oscilloscope was connected to monitor transient pulse widths. The equipment interfaced with a data acquisition system through a National Instruments<sup>®</sup> Data Acquisition Card and IEEE 488 Interface drivers.

The LabWindows<sup>®</sup> software programs used for data collection and analysis were written in C computer language and developed/modified in-house by several previous

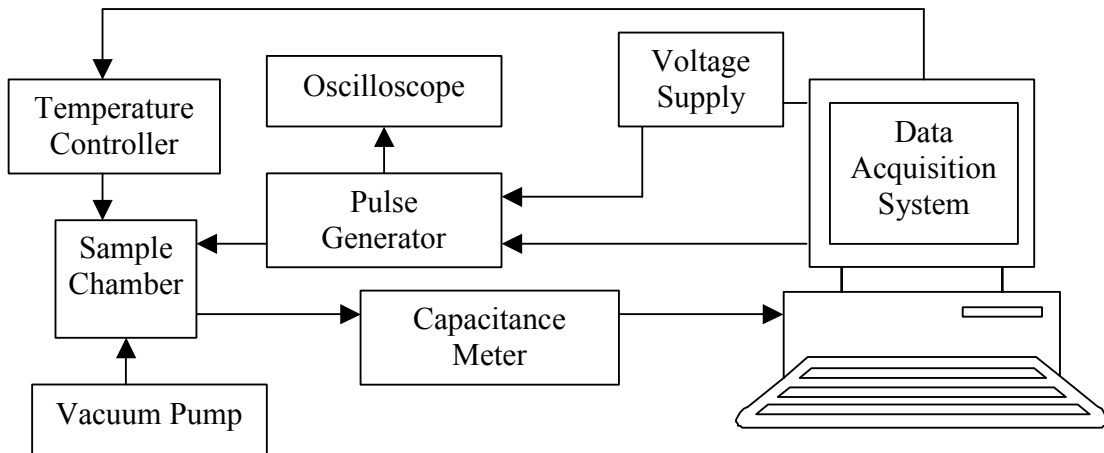


**Figure 11: Deep level transient spectroscopy laboratory set-up**

doctorial students during their dissertations [Scofield, Scott]. These programs include DLTS data acquisition software, a DLTS response fitting code, and an Arrhenius plotting program.

## **Chapter V : Data Analysis and Results**

The following chapter presents a summary of the data collected during this research. First, changes in the optical properties are discussed, addressing the existence of neutral nitrogen complexes in the near bandgap regions as well as the concept of phonon replica behavior. Following is a discussion of the effects of proton irradiation on the nitrogen-related peak structures in addition to the emergence of a radiation-induced peak structures as a result of proton bombardment. The effects of isochronal thermal annealing at 900, 1100, 1300, and 1500 °C on the shallow trap behavior concludes the section on optical measurements.

Next, changes in the electrical properties of SiC devices are discussed. The effects of proton irradiation on the rectifying characteristics of the fabricated Schottky barrier diodes are evaluated using I-V curve measurements. Terms to include saturation current, turn-on voltage and leakage current are used to describe changes in the material resistance, which directly affects the device's rectifying characteristics. Changes in the material resistance were investigated as a function of irradiation and subsequent thermal annealing.

Deep center formation in the material was probed using DLTS measurements. Initial characterization verified the introduction of defect centers as a result of proton irradiation. A summary of the DLTS system limitations is made in addition to a comparison of damage resulting in like 4H-SiC material due to neutron irradiation. After a discussion of the measured DLTS data as a function of proton irradiation and high-temperature annealing is completed, the validity of the curve fitting of the rate window

data is discussed. The capacitance peak is resolved using a multiple exponential fitting scheme to determine the trap parameters in the related proton-induced damage complex.

### **Photoluminescence Spectroscopy Data Analysis**

The optical emission spectrum of SiC can be very complex due to the existence of inequivalent lattice sites, which result in site-dependent ionization potentials for each impurity [Davis:17]. Hence, multiple radiative transitions are seen for the same impurity atoms with their corresponding phonon replica series. Figure 12 represents the photoluminescence spectrum (3.12 – 3.26 eV) measured from the as-grown nitrogen-doped (n-type) 4H-SiC. The zero phonon lines (ZPLs), due to neutral nitrogen-bound exciton recombinations [Choke, Scott:VI-79], are visible in the near band edge region ( $E_g = 3.28$  eV) and are marked as  $P_0$  and  $Q_0$ . In other words, they are the lines which are apparent as a result of exciton recombination without phonon emission at the two inequivalent un-ionized nitrogen donors.

The  $P_0$  peak, at a measured value of 3.257 eV, is attributed to the neutral nitrogen bound exciton at the hexagonal site while the  $Q_0$  peak, at a measured value of 3.244 eV, is associated to the cubic lattice site. The higher binding energy at cubic sites results in a more localized exciton and significantly increases the probability of recombination without momentum-conserving photons, which is evident by the intensity of the cubic-site ZPL ( $Q_0$ ) compared to the hexagonal-site ZPL ( $P_0$ ) [Scott:VI-79]. The energy spacing between the paired spectral lines is approximately 13 meV. The displacement of  $P_0$  from the exciton energy gap measures the binding energy of the exciton to the P

nitrogen donor. The disassociation energies of the exciton bound to the neutral nitrogen are approximately 9 and 20 meV for the hexagonal and cubic sites, respectively.

Phonon replica luminescent peaks of these ZPLs are apparent at several lower energies. Phonon emission, as a result of inelastic light scattering in crystals, is susceptible to selection rules originating from wave vector conservation [Harris:21]. In uniaxial crystals (SiC:c-axis), it is possible to observe these short-range inter-atomic forces between different lattice sites. As a result of the unique crystal structure (lattice

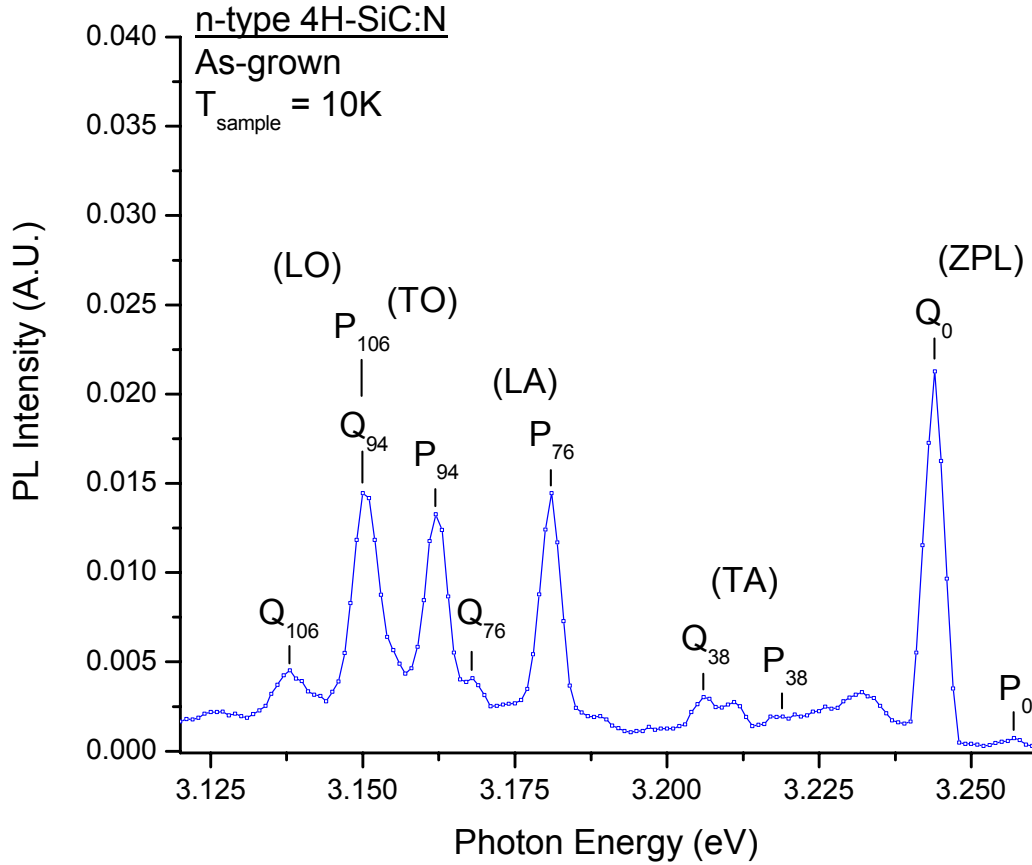


**Figure 12: Photoluminescence spectra of as-grown epitaxial n-type 4H-SiC. The zero phonon lines (ZPLs) and several corresponding phonon replicas associated with the neutral nitrogen complex are listed.**

stacking) of each SiC polytype, a common phonon spectrum is observed which depends solely on the atomic spacing [Harris:21-24]

Each pair of peaks observed in the 4H-SiC PL spectra is an example of these lattice-related phonon emissions and represents a set of phonon replicas generated as a result of the presence of the nitrogen-related excitons in the material. Peaks labeled with a P on Figure 12 denote recombinations of excitons bound to neutral nitrogen substituting at hexagonal sites while the Q-series denotes recombinations of excitons bound to neutral nitrogen substituting at cubic sites. The subscripts denote the energy spacing between the ZPL and the associated phonon energies.

Previous work conducted by Feldman et al. reported the energy spacing of lattice-related phonons characteristic to the 4H-SiC polytype. [Feldman] This group compared Raman spectra to study polytypic variations in the resultant phonon dispersion curves. However, first order Raman spectroscopy (RS) may only investigate phonons with a momentum wavevector ( $q$ ) approximately equal to zero [Harris:21] and therefore defines a reduced momentum,  $x = q/q_{\max}$ , which establishes the points of the phonon dispersion curves accessible by RS in extended  $\mathbf{k}$ -space [Fig. 13].

Feldman et al. approximate the transverse acoustic (TA), longitudinal acoustic (LA), transverse optical (TO), and longitudinal optical (LO) principle phonon energies at 33, 76, 93, and 104 meV, respectively. [Feldman:789] These phonon energies represent the weak long-wavelength vibrational mode located at  $x = 1$ . The phonon energies observed in this study show relatively excellent agreement at 38, 76, 94, and 106 meV, respectively. Several other phonon pairs (not represented in Figure 12) are also present at energy spacings of 23, 33, 81, and 117 meV. These peaks represent doubly degenerate

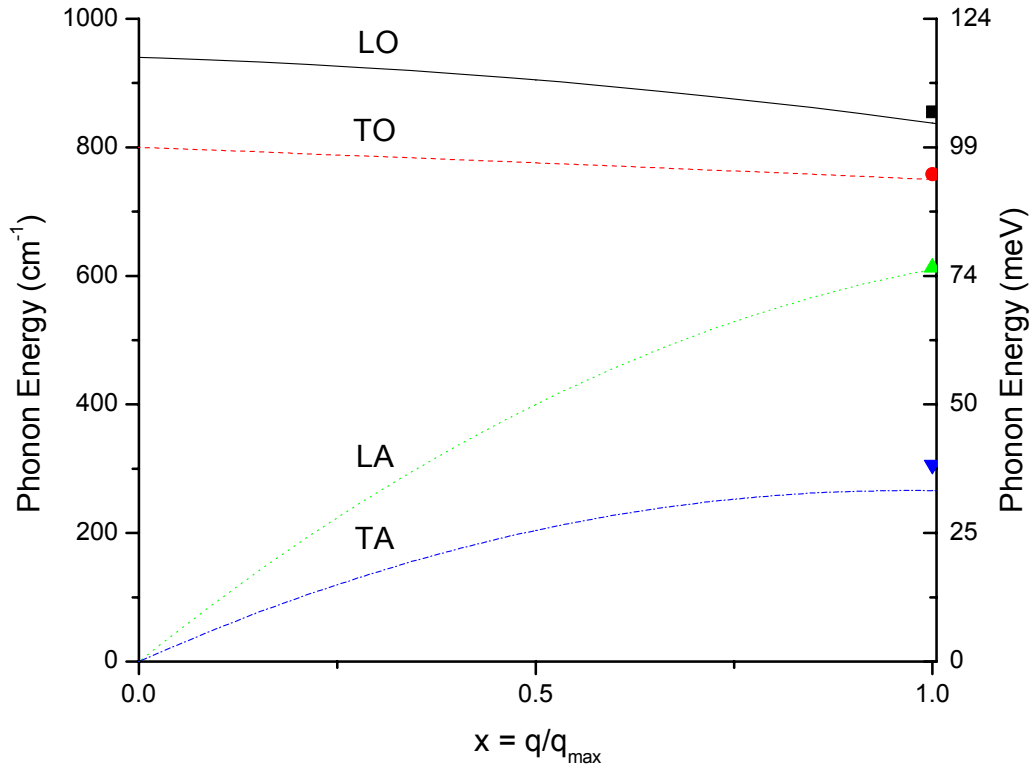


**Figure 13: The lattice-related phonon energies of 38, 76, 94, and 106 meV detected by photoluminescence measurements of the n-type 4H-SiC material (shown at right). The curves shown are reproduced from Feldman for the phonon energies for 4H-SiC along the c-axis.**

phonon branches (in the weak mode at  $x = 0.5$ ) due to SiC polytype anisotropy. [Feldman:789]

Figure 14 shows the progression of the n-type 4H-SiC PL spectra as the proton-irradiated material is annealed at various high temperatures. As the as-grown material is irradiated, the near band edge peaks ( $\sim 3.25$  eV) are attenuated while deeper, shallow-trap level PL peaks begin to emerge. The quenching of the nitrogen-associated ZPLs and associated phonon replicas may be caused by several material changes. First, the proton irradiation may be causing a reduction in the concentration of undamaged nitrogen sites,

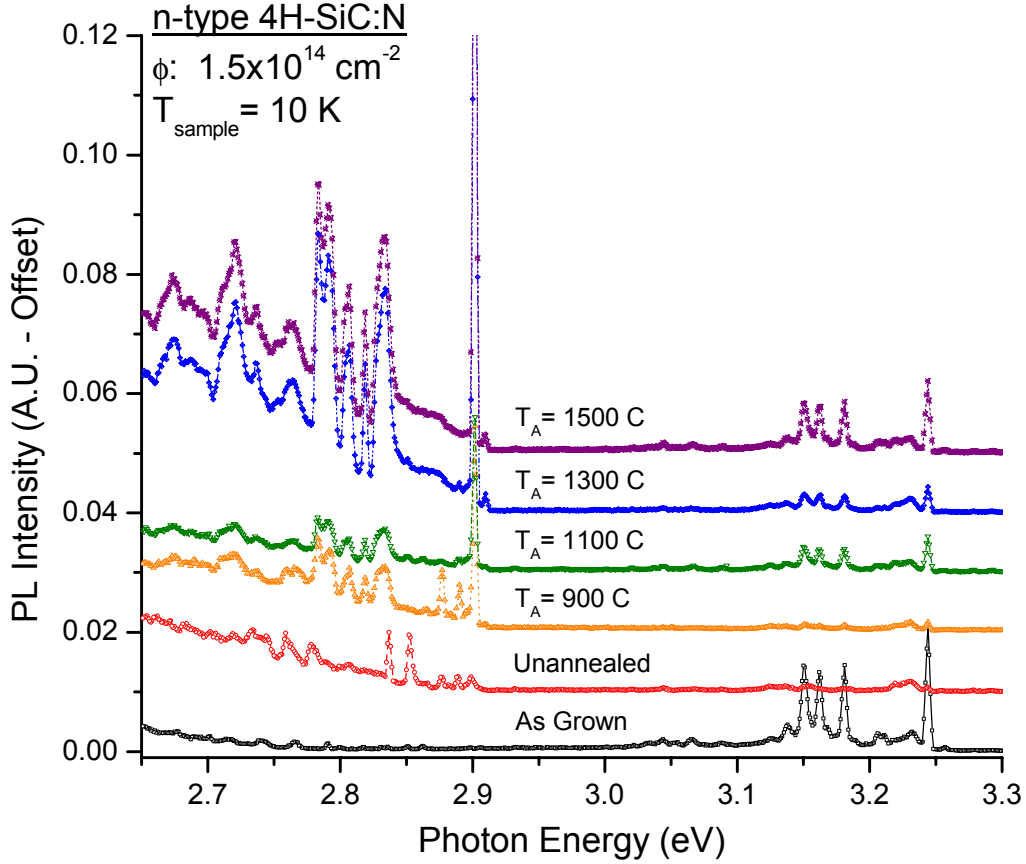


**Figure 14: Constant-temperature photoluminescence spectra of n-type 4H-SiC epilayers irradiated by 2 MeV protons (dose  $\sim 1.5 \times 10^{14} \text{ cm}^{-2}$ ) and subsequently annealed for 20 minutes at several temperatures. The spectra are offset for clarity.**

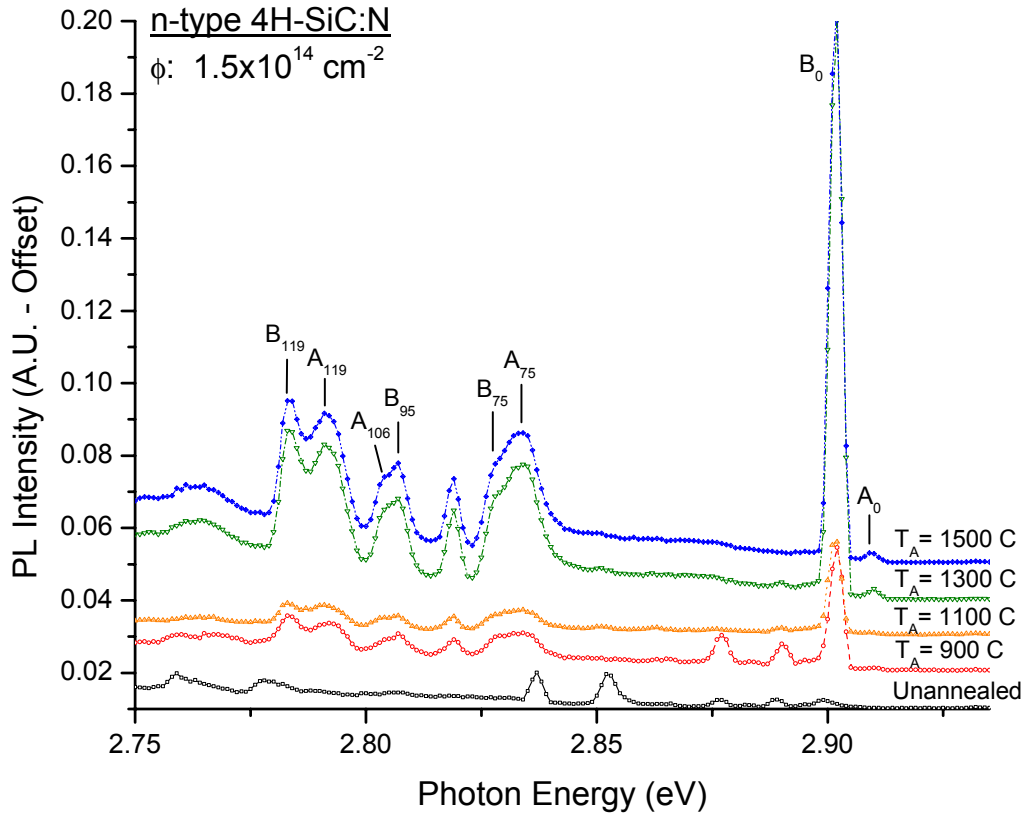
thereby altering the signal intensity relative to the noise signal. Another possibility may be that an increase in the probability of photon re-absorption has occurred due to an increase in absorbing defects. One or both of these processes could be taking place, causing the nitrogen-associated PL spectrum of irradiated SiC to diminish.

Figure 15 illustrates the evolution of the photon luminescence as a result of thermal annealing in irradiated material for trapping sites located deeper in the bandgap ( $E_C - E_T > 200 \text{ meV}$ ). Increasing the anneal temperature causes a nonlinear change in

luminescence in the energy region of 2.75 – 2.9 eV that is not seen in the near band edge region (~3.25 eV).

The unannealed, irradiated material shows a decrease in the emission spectrum as compared to as-grown material with almost total quenching of the near band edge characteristics and an increase in the broad green luminescence (2.7 – 2.9 eV). Visual inspection of the samples after irradiation showed a decrease in the transparency of the material, taking on a translucent olive coloring. This change in color is evident in the measured emission spectra and it may be an indication of the introduction of photon-absorbing trap centers within the bandgap.

Thermal annealing of the irradiated material at 900 °C for twenty minutes intensifies the signal of four peaks centered on 2.89 eV. Temperature-dependent PL measurements of these peaks indicate the existence of two defects, each associated with the hexagonal and cubic equivalent lattice sites. A set of two peaks, 2.837 and 2.852 eV respectively, become quenched in the growing green emission band luminescence. Upon annealing the irradiated material at 1100 °C for twenty minutes, the concentration of trapping centers at 2.890 and 2.895 eV are reduced below detectable levels and the relative intensity of the entire emission spectrum shown is decreases significantly. Such behavior suggests that shallow damage centers, introduced by the proton irradiation, are beginning to anneal out of the material. After annealing at 1300 °C, the emission PL peak intensities re-emerge with the appearance of a strong signal at 2.90 eV along with its associated phonon replicas. The signal is further enhanced after the damaged material is annealed at 1500 °C.



**Figure 15: Photoluminescence spectra of irradiated n-type 4H-SiC after subsequent high-temperature annealing at several temperatures. The spectra are offset for clarity.**

The resultant emission spectrum is dependant on two probability factors. The first of these is the probability that a recombination event will result in a radiative transition (versus de-excitation through non-radiation recombination). The second deals with the probability that the emitted photon is reabsorbed within the material, preventing it from being detected. This is especially true for the deeper trapping centers, resulting in a decrease in the signal intensity. The complexity of the measured spectrum response to anneal temperature increases even more since the concentration of defect centers, in

addition to the emission and capture probabilities, change as a function of annealing temperature, and those changes are not necessarily proportional to the change in temperature, or to one another. The re-emergence of the 2.90 eV peak structure with higher temperature annealing could be caused by an increase in the trap concentration, a decrease in the re-absorption cross-sections, or both.

Nevertheless, as the irradiated material is annealed, deep-level site activation becomes evident. A peak signal at 2.90 eV, which is not detected from as-grown material, appears due to irradiation and subsequently grows with thermal annealing. The  $A_0$  peak (2.910 eV) represents the defect-exciton transition most likely at the hexagonal site while the  $B_0$  peak (2.902 eV) represents the defect-exciton most likely transition at the cubic site. The A- and B-series denote recombinations associated with phonon replicas series of the  $A_0$  and  $B_0$  peaks, respectively.

The emergence of the 2.90 eV peak complex has been detected in other 4H-SiC material studies. Scott investigated changes in the optical and electrical properties of SiC as a result of ion-implantation damage. Using cathodoluminescence spectroscopy (similar in theory to PL), the same defect complex and associated phonon replica series are apparent in 4H material that has been implanted with argon and annealed at 1400 °C [Scott:VI-94 – VI-99]. Identical ZPL peaks are also detected in 4H material implanted with phosphorus. These findings suggest that this defect is damage-related and not due to any one of the implanted constituents.

As the photon peak intensity increases, so do the related phonon replica peak intensities. Lattice-related phonon replica peaks at 75, 95, 106, and 119 meV are clearly present in Figure 14. These energy spacings closely match the values uncovered in the

neutral nitrogen complex previously discussed. This consistent energy spacing between peaks is due to the 4H-SiC crystalline structure. Even though a defect center is located at different energy levels within the bandgap, the associated phonon replicas are dependent on the crystal structure (lattice-related).

Figure 16 illustrates the partial recovery of the near band edge characteristics with thermal annealing. For clarity, only data related to as-grown, irradiated/unannealed, and irradiated material after thermal annealing at 1500 °C is represented. Introduction of thermal energy to the crystal lattice, while stimulating the appearance of shallow traps

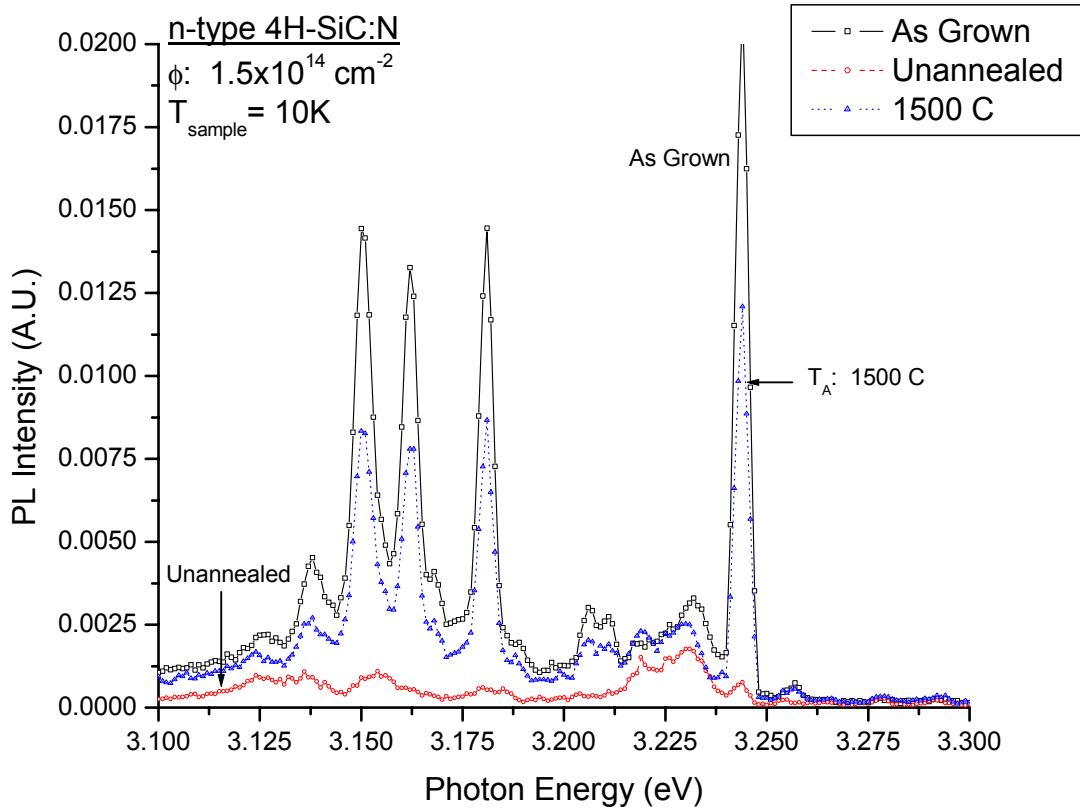


**Figure 16: Constant-temperature photoluminescence spectra of as-grown and irradiated epitaxial n-type 4H-SiC. Note the effect of high-temperature annealing (1500 °C) in the recovery of the intrinsic near-band edge phonon structure.**

deeper in the bandgap [reference Figure 14] also restores a significant portion of the nitrogen sites to the pre-irradiated conditions. Full recovery of the radiative properties of the nitrogen-associated peaks however, is not evident even after annealing at 1500 °C for twenty minutes. This is in agreement with a study completed by Storasta et al. which found that n-type 4H-SiC epilayers (CVD:20 µm) irradiated with 2.9 MeV protons showed complete recovery ( $N_T < 10^{12} \text{ cm}^{-3}$ ) only after thermal annealing at 1700 °C [Storasta].

#### Summary of the Optical Properties Characterization of 4H-SiC.

The near band edge characteristics of nitrogen-doped n-type 4H-SiC are present in the optical spectrum of the as-grown samples. The recombination events related to the neutral nitrogen bound exciton complex are clearly visible and serve as an indication of the quality of the CVD grown epitaxial material as well as a reference point in determining the energy spacing of the lattice-related phonons.

The material is altered as a result of proton irradiation by 2 MeV particles as the luminescence of these shallow centers is attenuated almost entirely with the emergence of deeper shallow traps at energies greater than 350 meV below the bandgap. Subsequent high-temperature thermal annealing of the material results in an increase in the emission spectrum at both the near band edge region ( $E_g \cong 3.25 \text{ eV}$ ) and between  $(E_C - E_T) = 2.65$  and 2.95 eV. Recovery of the characteristic nitrogen-related peaks at the near band edge following high-temperature annealing is identified, but is not complete at  $T_A = 1500 \text{ °C}$ .

In the deep trap region below 2.95 eV, activation of trap centers with annealing results in a sharp increase in the signal intensity of an irradiation-induced defect trap

(2.90 eV) as well as the associated phonon replicas. Based on previous ion-implantation studies in 4H-SiC conducted by Scott, the emergence of the 2.90 eV defect complex and associated phonon replicas may not be related to hydrogen implantation as a result of the proton irradiation, but instead as a result of the ensuing lattice damage.

## **Electrical and Deep Level Transient Spectroscopy Data Analysis**

### I-V Rectifying Characteristics.

In addition to changes in the optical properties of SiC, irradiation and subsequent high-temperature annealing had an effect on the electrical properties of the material. Measurements of the I-V characteristics of the Schottky barrier diodes were compared to evaluate changes in the 4H-SiC material resistance and rectifying behavior. Several separate diodes on each 5x5 mm sample were investigated over a voltage range of  $-1.0$  to  $0.3$  V. Each sample was then evaluated based on the data producing the greatest amount of leakage current under a  $-1.0$  V reverse bias.

Figure 17 represents the I-V curve behavior for the as-grown and irradiated 4H-SiC diodes. The as-grown material shows a maximum leakage current of less than  $35\text{ }\mu\text{A}$  at a reverse bias of  $-1.0$  V, providing an indication of the initial quality of the metal-semiconductor Schottky junction. The turn-on behavior for the sample indicates a forward bias value greater than  $0.3$  V. After irradiation, but prior to any thermal annealing, the rectifying capability of the SiC diodes increases. The leakage current is reduced to less than  $5\text{ }\mu\text{A}$  at  $-1.0$  V reverse bias and the device begins to turn on at a value less than  $0.3$  V. Upon annealing the sample for twenty minutes at  $900\text{ }^{\circ}\text{C}$ , the

device's rectifying characteristics further improve. The leakage current at  $-1.0$  V is less than  $-1$   $\mu\text{A}$  and the turn-on voltage of the device is significantly decreased to an approximate value of  $0.2$  V.

Increasing the annealing temperature to  $1100$   $^{\circ}\text{C}$ , however, causes the device's rectifying characteristics to degrade and the leakage current to increase, forming a nearly linear response to a reverse bias. At the higher anneal temperature of  $1300$   $^{\circ}\text{C}$ , the diode is no longer rectifying and exhibits purely ohmic behavior. This is why in the discussion on DLTS results, the samples annealed at  $1300$   $^{\circ}\text{C}$  are not included. A rectifying diode

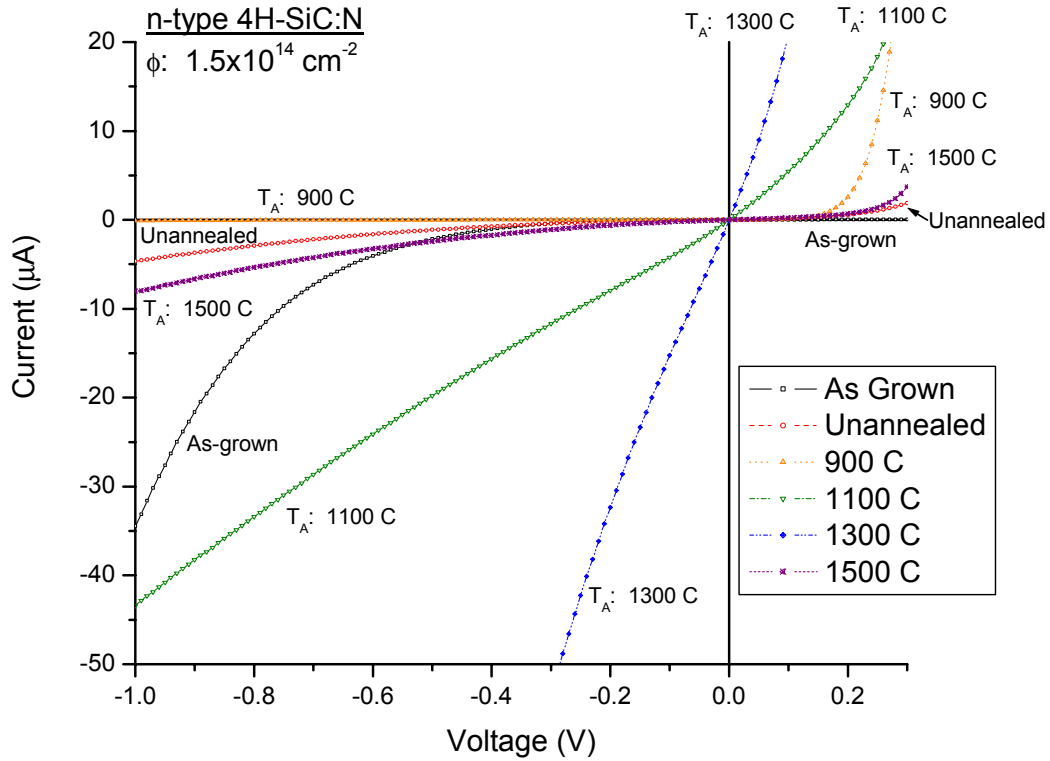


**Figure 17: Rectifying behavior of irradiated n-type 4H-SiC followed by thermal annealing at several temperatures**

could not be produced in the 1300 °C sample and no DLTS data could be measured.

Conversely, as the anneal temperature is increased to 1500 °C for twenty minutes, the diode regains a rectifying behavior once again, as the material shows signs of deep level damage recovery. The leakage current is slightly less than that of the as-grown, irradiated material, however the leakage and turn-on characteristics are still poorer than those presented in the irradiated material after thermal annealing at 900 °C.

### DLTS Results.

In this area of study, each n-type SiC device was tested over a DLTS temperature range of 175 – 575 K. Initially, I employed both modulating functions techniques and curve fitting of the rate window curves for post-test analysis to determine the trap parameters. These fitting programs were written by researchers at the Air Force Institute of Technology over the course of several research quarters [Scofield, Scott]. For a single trap center, this is an effective method for trap parameter extraction, however in the case of SiC, multiple defects form in close energetic level pairs and the resultant rate window curve is actually a summation of several sub-peaks. In order determine the unique trap parameters, the model requires the use of a multiple exponential summation. It was determined that the fitting programs did not provide the necessary flexibility to incorporate several (more than three) exponential curves fits [Scott:VI-12], therefore the trap parameters are determined manually. Although the manual fitting technique is more time- and labor-intensive than the modulating functions fitting programs, it was necessary in order to determine the defect levels and trap parameters associated for each rate window data curve with relative confidence in the findings.

Initial measurements of as-grown, annealed, and irradiated material showed no deep level defect activation at temperatures below 200 K, which is not surprising due to the carrier freeze-out (since the bandgap is so large). At temperatures greater than 575 K, all of the irradiated diodes had leakage current that exceeded the DLTS current limit. Most of the devices failed at even lower temperatures. The DLTS equipment utilizes a maximum leakage current limit of 100  $\mu\text{A}$  to ensure that the samples are operating without a significant concentration of free carriers in the depletion region. It is interesting to note that in a separate study, SiC samples taken from the same wafers and irradiated with a normalized spectrum of 1 MeV neutrons ( $1 \times 10^{14} \text{ cm}^{-2}$ ) did not exhibit the same leakage current problems, as each of these devices were sampled using CV-DLTS over a temperature range of 200 – 700 K [Jones]. These results may be related to the particle interaction mechanisms of the penetrating radiation. Protons interact, producing ionization and dislocation damage and because of their charged nature, they deposit a large portion of their energy within a relatively small volume. Conversely neutrons interact, for the most part, through kinetic displacement of lattice atoms. A higher concentration of damage sites close to the contact barrier could support greater conduction through the depletion region.

An example of several DLTS rate window curves for the annealed n-type 4H-SiC is presented in Figure 18. No deep level centers are detected above the sensitivity levels of the DLTS equipment ( $\sim 10^{-5} \times (N_D - N_A)$ ), over a temperature range of 175 – 575 K for as-grown and non-irradiated annealed samples. This suggests that any trap levels detected within this temperature region are created via the proton irradiation and then enhanced or suppressed due the high-temperature annealing processes.

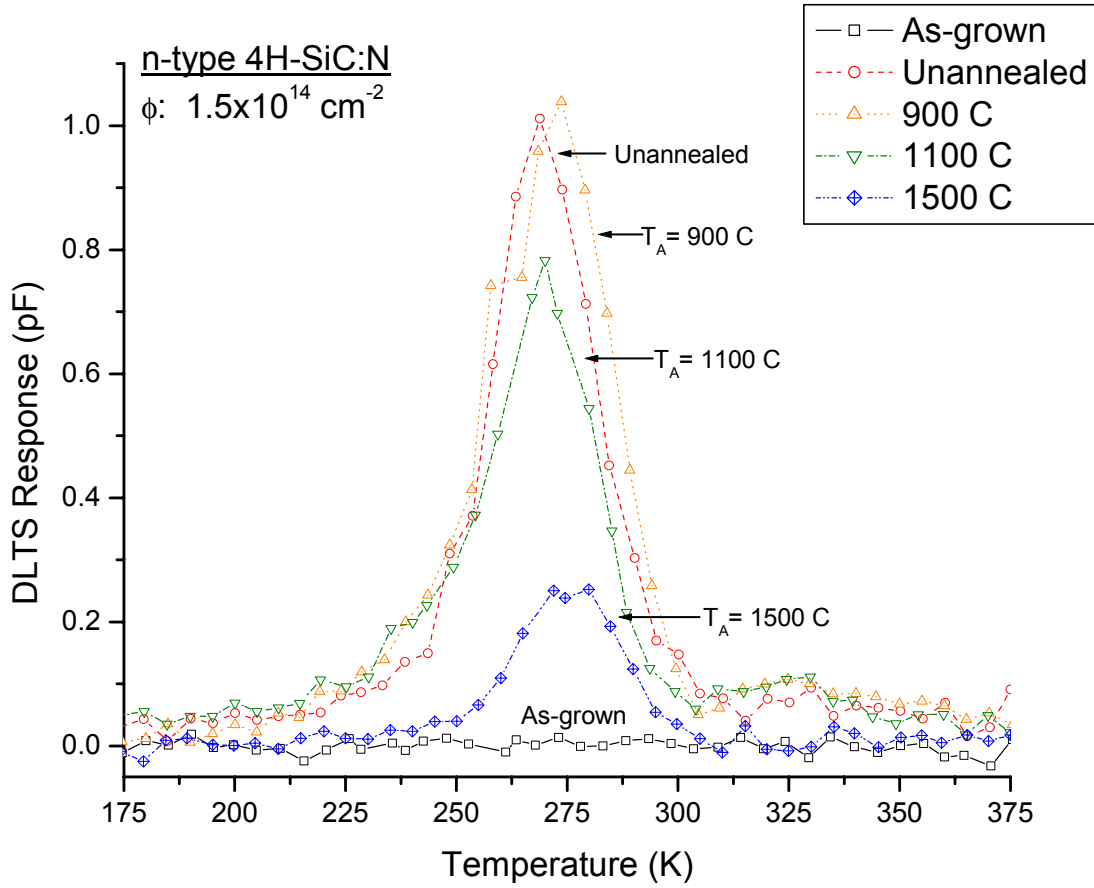


**Figure 18: DLTS response curve of n-type 4H-SiC illustrating the emergence of deep centers as a result of proton irradiation. Note the decrease in peak signal as a result of high-temperature annealing.**

A single deep level defect pair is evident in the irradiated 4H-SiC material, activating between the temperatures of 280 – 310 K. The rate window is determined by the start and stop time of the recorded transient capacitance ( $t_1 = 40$  ms and  $t_2 = 335$  ms). A comparison between the as-grown (noise level) response curve with the proton-irradiated response curve establishes the introduction of deep level trap centers due to irradiation. Furthermore, the signal intensity does not diminish as a result of thermal annealing at 900 °C for twenty minutes. The rate window curve of an irradiated sample

after annealing at 1100 °C however, demonstrates a decrease in the defect level trap concentration within the probed SCR, though complete recovery of the trapping center is not apparent even after annealing at 1500 °C.

In order to evaluate the trap parameters, it was necessary to use a manual curve-fitting algorithm. The algorithm was set up in ORIGIN<sup>®</sup> 6.1 and an example of the curve parameters are presented in Figure 19. The solid line represents the measured data, each of the dashed lines represent each of the unique defect centers and the asterisked line represents the summation of the sub-peaks.

Each defect peak may be uniquely characterized by the trap energy, the capture cross-section, and the trap concentration. The trap parameters associated with each individual sub-peak are listed at the right in Figure 19. These parameters affect: 1) the peak placement; 2) the full width half max (FWHM) of the peak and; 3) the peak height. Matching the individual trap characteristics to produce a sum peak, which corresponds exactly to the measured data, requires a specific series of sub-peaks.

Some error is present in the fitted curve data as a result of poor measured data resolution. The DLTS data was measured in temperature steps of 5 K, which has proven to be too large a data measurement step. Greater peak resolution is possible using smaller temperature steps (~ 2 K steps), permitting a better fit of the data. However, decreasing the temperature step increases the time of DLTS data acquisition, which is already a time-intensive process.

Each of the rate window curves for the irradiated n-type material were characterized using the manual curve-fitting algorithm. Tables 5 through 8 outline these experimentally determined defect centers and their associated trap parameters for the SiC

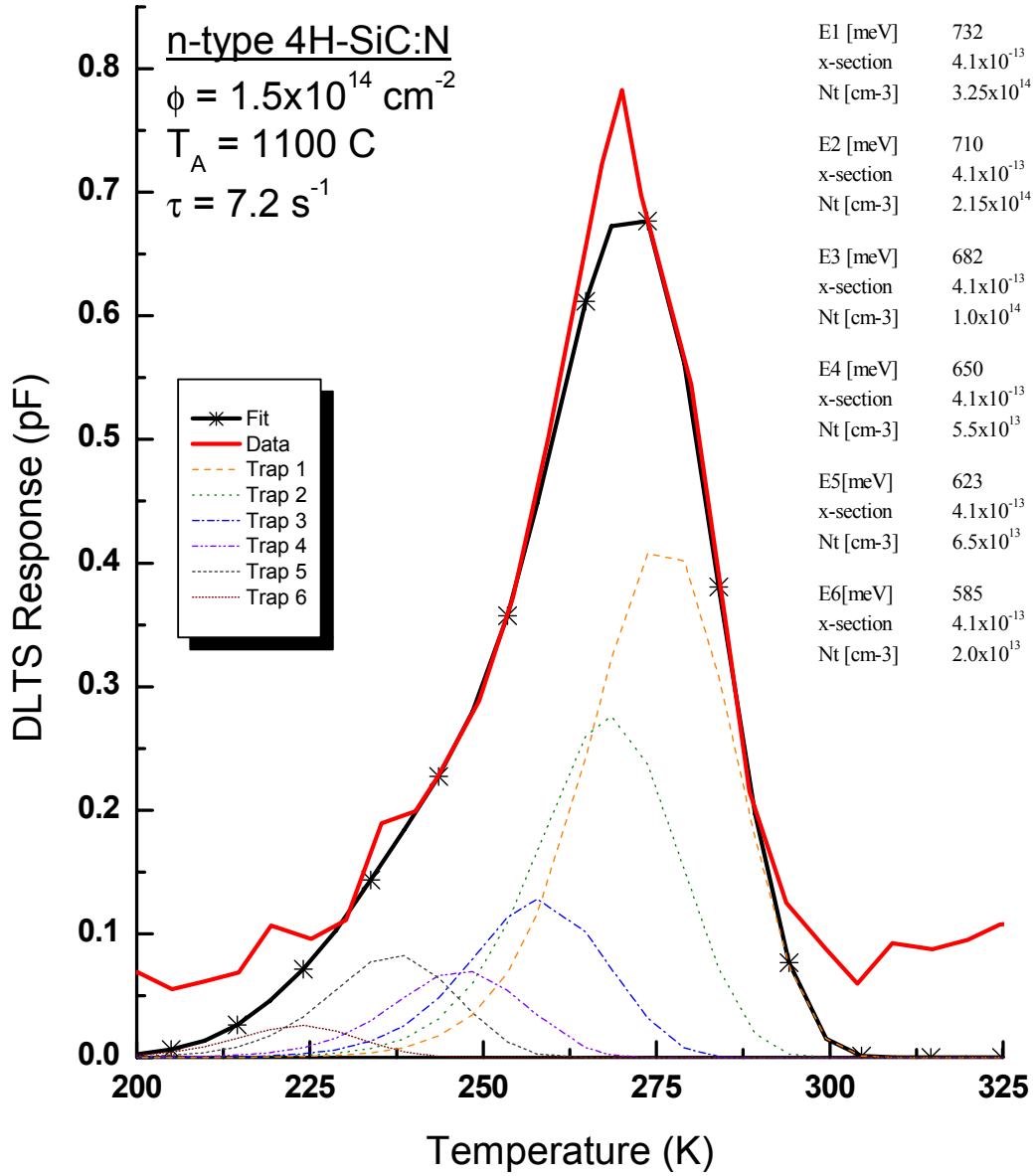


**Figure 19: DLTS response curve for n-type 4H-SiC material, irradiated and annealed at 1100 °C. Using a manual curve-fitting algorithm, the data peak is resolved into six individual trapping centers. The associated trap parameters, ( $E_T$ ,  $\sigma_T$ ,  $N_T$ ) for each defect peak are listed at right.**

samples in each anneal step. The first column lists the temperature at the peak maximum, column two lists the energy level of the trap, the third column lists the capture cross-

section of the trap, and the fourth column gives the concentration of trapping centers. As a result of the decreased DLTS data resolution, only the two largest sub-peaks were resolved for the unannealed material and the material annealed at 1500 °C.

**Table 5: Trap parameters of proton-irradiated n-type 4H-SiC prior to thermal anneal**

$T_{\text{Peak}}$ (K)	Energy (meV)	$\sigma_T$ (cm <sup>-2</sup> )	Density (cm <sup>-3</sup> )
265	701	$5.0 \times 10^{-13}$	$2.35 \times 10^{14}$
273	731	$5.0 \times 10^{-13}$	$5.90 \times 10^{14}$

**Table 6: Trap parameters of proton-irradiated n-type 4H-SiC annealed at 900 °C**

$T_{\text{Peak}}$ (K)	Energy (meV)	$\sigma_T$ (cm <sup>-2</sup> )	Density (cm <sup>-3</sup> )
217	567	$3.7 \times 10^{-13}$	$3.00 \times 10^{13}$
227	598	$3.7 \times 10^{-13}$	$6.00 \times 10^{13}$
243	638	$3.7 \times 10^{-13}$	$1.00 \times 10^{14}$
257	678	$3.7 \times 10^{-13}$	$1.45 \times 10^{14}$
267	710	$3.7 \times 10^{-13}$	$2.80 \times 10^{14}$
277	735	$3.7 \times 10^{-13}$	$5.60 \times 10^{14}$

**Table 7: Trap parameters of proton-irradiated n-type 4H-SiC annealed at 1100 °C**

$T_{\text{Peak}}$ (K)	Energy (meV)	$\sigma_T$ (cm <sup>-2</sup> )	Density (cm <sup>-3</sup> )
225	585	$4.1 \times 10^{-13}$	$2.00 \times 10^{13}$
237	623	$4.1 \times 10^{-13}$	$6.50 \times 10^{13}$
245	650	$4.1 \times 10^{-13}$	$5.50 \times 10^{13}$
257	682	$4.1 \times 10^{-13}$	$1.00 \times 10^{14}$
267	710	$4.1 \times 10^{-13}$	$2.15 \times 10^{14}$
275	732	$4.1 \times 10^{-13}$	$3.25 \times 10^{14}$

**Table 8: Trap parameters of proton-irradiated n-type 4H-SiC annealed at 1500 °C**

$T_{\text{Peak}}$ (K)	Energy (meV)	$\sigma_T$ (cm <sup>-2</sup> )	Density (cm <sup>-3</sup> )
270	707	$2.8 \times 10^{-13}$	$8.30 \times 10^{13}$
279	732	$2.8 \times 10^{-13}$	$1.40 \times 10^{14}$

For example, the two largest defect centers, observable in each of the sample sets, have a maximum peak temperature of approximately 275 and 267 K, respectively. The trap energies are approximately 730 and 710 meV (from the conduction band) for unannealed, 900 °C, 1100 °C, and 1500 °C thermally annealed sample material. These two peaks most likely represent a defect pair relating the inequivalent sites in the 4H-SiC material with an energy spacing of approximately 25-30 meV. The ratio in defect pair concentrations ranged from 3:1 to 1.5:1 with the deep trap of each pair having the larger concentration. Evaluating the trap parameters as a function of anneal temperature, the capture cross-sections of the traps change very little, however the concentration of defects decreased as the anneal temperature was increased.

#### Summary of the Electrical Properties Characterization of 4H-SiC.

The electrical characterization of 4H-SiC Schottky diodes confirms the existence of deep level defects induced by proton irradiation of 2 MeV particles. It is interesting to note that the I-V measurements indicate an enhancement of the rectifying characteristic of these diodes with irradiation, followed by high-temperature thermal annealing at 900 °C. The samples annealed at 1100 °C showed degradation in the rectifying qualities of the SiC devices as well as the samples annealed at 1300 °C, which were so damaged that deep level characterization was impossible. Some of the rectifying response behavior is recovered after thermal annealing at 1500 °C.

The DLTS rate window curves reveal the presence of a deep level trap cluster, activating between 200 and 300 K. Measurement of as-grown/annealed material confirms that the deep-level traps in the irradiated material are induced by proton

interaction in the material. The trap parameters are found by analyzing the rate window curves using a manual curve-fitting algorithm in ORIGIN<sup>®</sup>. The traps formed as a result of proton irradiation do not exhibit a significant change in the trap energy or capture cross-section parameters as a function of anneal temperature, but they do demonstrate recovery with a decrease in trap density as the anneal temperature increases.

## Chapter VI : Conclusions and Closing Remarks

### Summary of Conclusions

In an effort to evaluate the potential application of 4H-SiC for space-based electronic systems, I investigated the optical and electrical behavior of proton-irradiated 4H-SiC material. The 4H-SiC was irradiated with 2 MeV protons (dose  $\sim 1.5 \times 10^{14} \text{ cm}^{-2}$ ), followed by high-temperature thermal anneals over a range of 900 °C to 1500 °C. The introduction of damage-related trapping centers is confirmed through the use of low-temperature photoluminescence (PL) and constant-voltage deep level transient spectroscopy (DLTS) characterization methods. Changes in the material resistance are evaluated using I-V curve measurements.

Irradiation with protons introduces both shallow and deep trap centers. The optical emission spectrum of the neutral nitrogen-related complex associated with n-type 4H-SiC is observed in as-grown material but is suppressed as a consequence of irradiation. Recovery of the signal is induced by high-temperature annealing, but is not fully recovered even after a twenty minute anneal at 1500 °C. Trap centers at energies greater than 350 meV below the bandgap are introduced and subsequently activated due to thermal annealing. A cubic/hexagonal-related defect pair is clearly distinguishable at 2.90 eV, ( $E_c - E_T$ ) = 0.38 eV, as well as its related phonon replicas.

Initial assessments of the rectifying characteristics of irradiated SiC showed signs of device enhancement, with an initial decrease in the reverse leakage current and device turn-on voltage. The best characteristics are exhibited in irradiated Schottky devices after

thermal annealing at 900 °C. However, the deep level trap characteristics exhibited in the DLTS rate window response curve do not show a significant change in the trap parameters between the unannealed and 900 °C annealed material, indicating the deeper level traps are responsible for the I-V characteristics.

The device characteristics after annealing at 1100 °C show a distinct reduction in the rectifying characteristics, resulting in an almost linear reverse leakage current behavior and immediate turn-on in the forward bias region. While the diodes became less efficient, DLTS measurements were still possible, but device failure due to the maximum allowable leakage current limit of the system was brought about at lower sample temperatures ( $T < 550$  K). The rate window response of the DLTS data for these samples showed a decrease in the concentration of defects as a result of thermal recovery.

As a consequence of thermal annealing at 1300 °C, the rectifying behavior of the Schottky devices is lost entirely and the sample acts as a conductor. It is because of this, that no DLTS response curves could be measured in the material. Instead of inducing a SCR under reverse bias, free-carrier injection occurred in the material at the contact interface. The device characteristics showed recovery of the rectifying behavior after thermal annealing at 1500 °C. The DLTS response curves generated for 1500 °C annealed material showed further decrease in defect concentrations of the defect pairs.

The 2 MeV proton irradiation of the 4H-SiC material at a dose of  $1.5 \times 10^{14} \text{ cm}^{-2}$  (approximate satellite lifetime of 5 years) caused significant changes in both the optical and electrical properties of the material. Damage-related luminescent peaks are detected through PL characterization. An enhancement of the rectifying behavior of the SiC Schottky devices was seen as a result of irradiation and thermal annealing at 900 °C.

Finally, the creation of deep-level defects was observed as a result of the proton irradiation. PL characterization confirms the emergence of a defect pair, centered at  $E_C - E_T = 380$  meV, which seems to be characteristic to the particle damage in SiC, independent of the damaging particle. Activation of the defect pair is observed as a result of thermal annealing. Deeper level traps are detected using DLTS characterization, with trap energy levels ranging from 570 – 730 meV below the conduction band. The trap parameters were evaluated using a manual curve-fitting algorithm to match a series sum of exponential curves to the measured data. With increasing thermal anneal temperature, a decrease in the defect concentration of the defect pairs was observed.

### **Proposals for Future Research**

As a result of the findings of this study regarding the potential of silicon carbide for high-temperature, high-radiation field environments, further research is warranted. The work done here serves only as an initial review of the material characteristics and potential applications of 4H-SiC in space-based radiation environments, providing a single datum point in the study of wide bandgap materials for future aerospace and space application systems. The potential exists for expanding the study and analysis of silicon carbide at the Air Force Institute of Technology. The following proposals summarize research topics, which encompass entire thesis/dissertation studies in and of themselves. The effort could be broken down even further to accommodate the research of several students in a single year.

### Low-temperature Anneal Study of SiC.

The findings of this research indicates that there may be an increase in the efficiency of the rectifying behavior of 4H-SiC diodes due to irradiation and subsequent annealing at temperatures lower than 1100 °C. This hypothesis is based on several I-V measurements of irradiated samples which have been annealed from 900 °C to 1500 °C. It is possible that decreased leakage current and lower turn-on voltages are achievable for samples experiencing thermal annealing at lower temperatures. Research conducted previously in 4H- and 6H-SiC indicates that defects induced by hydrogen implantation show signs of recovery after thermal anneals at temperatures below 400 °C [Storasta, Lebedev (2)]. I could not incorporate these temperatures in my anneal study due to the metal contact processing required of the DLTS and I-V characterization methods. Since the ohmic contacts of the Schottky diode required annealing at 900 °C, a probe of the defect formation and/or mobility behavior at lower temperatures could not be completed. Such an investigation would require a re-examination of the metallization processes or possible characterization through the use of non-contact analysis methods.

### Extended Proton Damage Study.

Due to a lack of time and resource availability only a partial study of the effects of proton irradiation over a range of doses and anneal temperatures was completed. This study made use of preliminary dose/damage data by irradiating eight samples (four n-type and four p-type) over a dose range of  $10^{12} - 10^{15} \text{ cm}^{-2}$  in order to estimate a fluence value that would induce measurable damage, but would not overwhelm the material and make it difficult to complete electrical characterization measurements. Now that an

investigation of the anneal behavior of irradiated material has been completed for a single dose, it would be prudent to conduct a study which varies: 1) the particle fluence; 2) particle energy or; 3) both impinged onto the material.

#### Proton Damage Profiling.

A profile of the proton damage peak in as-grown and thermally annealed 4H-SiC would provide additional insight into the introduction and mobility of trapping centers. Optical characterization may be completed using cathodoluminescence (CL) spectroscopy resources located at AFIT. Electrical measurements are possible through the use of double-correlated DLTS spectroscopy (DD-DLTS.) These, as well as other C-V characterization methods, may provide information helpful in distinguishing between defect types, changes in trap concentrations (due to activation or recombination), and the trap emission and capture cross-sections as a function of thermal annealing temperature.

In addition to trap identification, this data may be used to: 1) evaluate existing modeling codes used for ion implantation damage simulations (S-TRIM), or; 2) develop new modeling codes which provide at least a first-order approximation of the damage induced by energetic charged particle interaction. The development and verification of such a model would advance AFIT's capabilities to simulate more complex semiconductor device structures (oxide interfaces, P-N junctions, MOSFET, etc.) over a spectrum of charged particle energies and densities.

## Appendix: Photolithography Processing and Metallization

### Research:

Characterization of the Optical and Electrical Properties of Proton-Irradiated 4H-Silicon Carbide

### Substrate Material:

4H-SiC epilayer on a 4H-SiC bulk substrate

### Sample ID:

AG0746-03 (n-type), A0528-06Q (p-type)

### Name:

Heather Crockett, 2Lt, USAF

### Date:

Fall 2001

### Summary Statement:

The following recipe may be used to fabricate 4H-SiC Schottky barrier diodes.

\*\*\*\*\*

- 1) Clean substrate material with Trichloroethylene, Acetone, and Methanol  
Time: 30 seconds each (with no drying in between)  
Nitrogen dry
- 2) Hotplate bake 5 minutes @ 100 °C
- 3) Acid etch using heated 3:1 aqua-regia (HCl:HNO<sub>3</sub>) solution  
Temperature: 100 °C  
Etch time: 30 – 60 seconds  
Rinse: 30 seconds (deionized water)  
Nitrogen dry
- 4) Place into metal evaporator immediately to prevent SiO<sub>2</sub> build-up
- 5) Backside contact metal evaporation:  
N-type Ohmic  
First Layer: Nickel  
Thickness: 2000 Å  
  
P-type Ohmic  
First Layer: Titanium  
Thickness: 200 Å

Second Layer: Aluminum  
Thickness: 1800 Å

- 6) Ohmic anneal:  
N-type: Tube Furnace  
Time: 5 minutes  
Temperature: 900 °C  
Gas atmosphere: Nitrogen  
  
P-type: RTA Furnace  
Time: 2 minutes  
Temperature: 900 °C  
Gas atmosphere: Nitrogen
- 7) Test for Ohmic contact  
Current: < 1 mA  
Voltage: -0.5 to 0.1 V  
NOTE: If contact does not exhibit ohmic ( $V = IR$ ) characteristics, repeat steps 6 and 7
- 8) Clean substrate material with Trichloroethylene, Acetone, Methanol  
Time: 30 seconds each (with no drying in between)  
Nitrogen dry
- 9) Hotplate bake 5 minutes @ 100 °C
- 10) Spin on 1813 Photoresist  
RPM: 6000  
Time: 30 seconds.
- 11) Hotplate bake 5 minutes @ 100 °C
- 12) Expose on mask aligner  
Mask layer: DLTS Ohmic  
Wavelength: 420 nm  
Exposure time: 60 seconds
- 13) Develop using 351 Microposit developer and DI water (DI : 351 (5:1))  
Speed: 1000 RPM  
Developer time: 30 seconds  
DI water rinse  
Nitrogen dry
- 14) Inspect under microscope to ensure substrate is developed
- 15) Metal evaporation:

N-type Schottky

First Layer: Titanium

Thickness: 2000 Å

P-type Schottky

First Layer: Titanium

Thickness: 2000 Å

- 16) Metal lift-off:  
Acetone bath  
Time: 5 minutes
- 17) Inspect under the microscope to see if metal has lifted in the correct field area.
- 18) Clean substrate material with Acetone, Methanol  
Time: 30 seconds each (with no drying in between)  
Nitrogen dry
- 19) Hotplate bake 5 minutes @ 100 °C

## Bibliography

Blood, P., Orton, J.W., Electrical Characterization of Semiconductors: Majority Carriers and Electron States, The, New York, Academic Press. 1992

Choke, W.J., Patrick, L., *Exciton Recombination Radiation and Phonon Spectrum of 6H-SiC*, Physical Review, Vol 127(6), p 1868, September 1962

Cree, Inc., *Silicon Carbide: Product Specifications*, Cree Research, Inc., 1998-2000

Davis, W. A., "Photoluminescence Spectroscopy of 4H- and 6H-SiC," MS thesis, AFIT/GAP/ENP/94D, Department of the Air Force, Air University, Air Force Institute of Technology, December 1994 (AD-A289326)

Dunn, M.E., "Electrical characterization of 4H-Silicon Carbide P-N Junction Diodes," MS thesis, AFIT/GAP/ENP/95D-04, Department of the Air Force, Air University, Air Force Institute of Technology, December 1995 (AD-A309857)

Feldman, D.W., et al., *Phonon Dispersion Curves by Raman Scattering in SiC, Polytypes 3C, 4H, 6H, 15R, and 21R*, Physical Review, Vol. 173(3), p.787, September 1968

Harris, G., Properties of Silicon Carbide, Materials Science Research Center of Excellence, Howard University, Short Run Press Ltd., England, 1995

Holmes-Seidle, A., Adams, L., Handbook of Radiation Effects, New York, Oxford University Press, 1993

Ingram, D.C., Director, Edwards Accelerator Facility, Ohio University, Athen Ohio, Personal Correspondence, 18 January 2002

Jones, K., "Measurements of Neutron-Induced Surface and Bulk Defects in 4H Silicon Carbide", MS thesis (Unpublished), AFIT/GNE/ENP/02M-03, Department of the Air Force, Air University, Air Force Institute of Technology, March 2002

Knoll, G.F., Radiation Detection and Measurement, New York: John Wiley & Sons, Inc., 1989

Lebedev, A.A., et al., *Doping of n-type 6H-SiC and 4H-SiC with defects created with a proton beam*, American Institute of Physics, July 2000

Lebedev, A.A., et al., *Radiation Defects in n-4H-SiC Irradiated with 8-MeV Protons*, MAIK (Russian Academy of Sciences), "Nauka/Interperiodica", February 2000

Messenger, G.C., Ash, M.S., The Effects of Radiation on Electronic Systems, 2<sup>nd</sup> Ed., New York, Van Nostrand Reinhold, 1992

Neudeck, P.G., *Benefits of Silicon Carbide Electronics to Commercial and Planetary Spacecraft*, <http://www.lerc.nasa.gov/WWW/SiC/spacebenefit.html>, National Aeronautics and Space Administration Lewis Research Center, December 2001

Neudeck, P.G., *Recent Progress in Silicon Carbide Semiconductor Electronics Technology*, <http://www.grc.nasa.gov/WWW/SiC/SiCReview.html>, National Aeronautics and Space Administration Lewis Research Center, October 1995

Schroder, D.K., Semiconductor Material and Device Characterization, 2<sup>nd</sup> Ed., New York, John Wiley & Sons, Inc., 1998

Scofield, J.D., “Electrical Characterization of Intrinsic and Induced Deep Level Defects in Hexagonal SiC”, PhD Dissertation, AFIT/DS/ENP/96-08, Department of the Air Force, Air University, Air Force Institute of Technology, November 1996 (AD-A325121)

Scott, M.B., “Electrical and Optical Characterization of Intrinsic and Ion-Implantation Induced Defects in 6H- and 4H-SiC”, PhD Dissertation, AFIT/DS/ENP/99-04, Department of the Air Force, Air University, Air Force Institute of Technology. November 1999 (AD-A371042)

Storasta, L., et al., *Proton Irradiation Induced Defects in 4H-SiC*, Materials Science Forum, “Silicon Carbide and Related Materials”, 2001

Sze, S.M., Physics of Semiconductor Devices, 2<sup>nd</sup> Ed., New York, John Wiley & Sons, Inc., 1981

Vichare, M., “Characterization of Silicon Carbide Power Semiconductor Devices for High Temperature Operation”, MS thesis, Wright State University, 1996

REPORT DOCUMENTATION PAGE				Form Approved OMB No. 074-0188	
<p>The public reporting burden for this collection of information is estimated to average 1 hour per response, including the time for reviewing instructions, searching existing data sources, gathering and maintaining the data needed, and completing and reviewing the collection of information. Send comments regarding this burden estimate or any other aspect of the collection of information, including suggestions for reducing this burden to Department of Defense, Washington Headquarters Services, Directorate for Information Operations and Reports (0704-0188), 1215 Jefferson Davis Highway, Suite 1204, Arlington, VA 22202-4302. Respondents should be aware that notwithstanding any other provision of law, no person shall be subject to a penalty for failing to comply with a collection of information if it does not display a currently valid OMB control number.</p> <p><b>PLEASE DO NOT RETURN YOUR FORM TO THE ABOVE ADDRESS.</b></p>					
1. REPORT DATE (DD-MM-YYYY)		2. REPORT TYPE		3. DATES COVERED (From – To)	
26-03-2002		Master Thesis		Aug 2001 – March 2002	
4. TITLE AND SUBTITLE  Characterization of the Optical and Electrical Properties of Proton-Irradiated 4H-Silicon Carbide				5a. CONTRACT NUMBER	
				5b. GRANT NUMBER	
				5c. PROGRAM ELEMENT NUMBER	
6. AUTHOR(S)  Crockett, Heather C., Second Lieutenant, U.S. Air Force				5d. PROJECT NUMBER	
				5e. TASK NUMBER	
				5f. WORK UNIT NUMBER	
7. PERFORMING ORGANIZATION NAME(S) AND ADDRESS(ES)  Air Force Institute of Technology Graduate School of Engineering and Management (AFIT/EN) 2950 P Street, Building 640 WPAFB OH 45433-7765				8. PERFORMING ORGANIZATION REPORT NUMBER  AFIT/GNE/ENP/02M-01	
9. SPONSORING/MONITORING AGENCY NAME(S) AND ADDRESS(ES)  Air Force Institute of Technology Graduate School of Engineering and Management (AFIT/EN) 2950 P Street, Building 640 WPAFB OH 45433-7765				10. SPONSOR/MONITOR'S ACRONYM(S)	
				11. SPONSOR/MONITOR'S REPORT NUMBER(S)	
12. DISTRIBUTION/AVAILABILITY STATEMENT APPROVED FOR PUBLIC RELEASE; DISTRIBUTION UNLIMITED.					
13. SUPPLEMENTARY NOTES					
14. ABSTRACT <p>Epitaxial n-type 4H-silicon carbide (SiC) is irradiated with 2 MeV protons to evaluate the dislocation damage effects on the optical and electrical characteristics of the material. Semiconductor materials with a high tolerance to radiation fields have applications in several aerospace power and satellite systems. SiC is under investigation due to its potential for such space material applications. The optical properties of the material are investigated using temperature-dependant photoluminescence (PL) and the effects of proton irradiation on the electrical properties are evaluated using current-voltage measurements and constant-voltage deep level transient spectroscopy (CV-DLTS). Subsequent high-temperature thermal annealing and recovery of the irradiated material is investigated over the temperature range of 900 – 1500 °C.</p> <p>Proton-induced irradiation damage is apparent in the 4H-SiC material, affecting both the optical and electrical characteristics of the devices. The radiative behavior of the nitrogen-related near band edge transitions is significantly reduced as a result of the irradiation with partial recovery observed after high-temperature thermal annealing at 1500 °C. A deeper trapping complex (<math>E_C-E_T \cong 380</math> meV) is detected as a result of irradiation and shows signs of activation due to thermal annealing. Initial indications taken from I-V measurements of the Schottky diodes reveal that proton irradiation followed by thermal annealing at 900 °C may, in fact, enhance the rectifying device characteristics. Increasing the anneal temperature (<math>T_A = 1300</math> °C) causes the device to fail entirely. Further annealing of the irradiated 4H-SiC at 1500 °C demonstrates recovery in the rectifying behavior of the material.</p> <p>Significant levels of deep level donor traps are observed, induced by irradiation in n-type material. Three detectable defect pairs emerge with energy levels ranging from 570 – 730 meV below the conduction band. The trap parameters were determined using curve-fitting algorithms. Upon high-temperature thermal annealing of the material, the trap center pairs showed little change in the energy levels and capture cross-sections while the density of traps decreased as temperatures increased. Full recovery of the material characteristics is not apparent after annealing at 1500 °C.</p>					
15. SUBJECT TERMS <b>4H-SiC, Proton, Photoluminescence, Deep level transient spectroscopy, Thermal anneal, Irradiation, Defects, Color centers</b>					
16. SECURITY CLASSIFICATION OF:			17. LIMITATION OF ABSTRACT	18. NUMBER OF PAGES	19a. NAME OF RESPONSIBLE PERSON
a. REPORT	b. ABSTRACT	c. THIS PAGE			19b. TELEPHONE NUMBER (Include area code)
U	U	U	UU	85	Maj Michael B. Scott, ENP (937) 255-3636 x4505